

Robust Trajectory and Resource Optimization for Communication-assisted UAV SAR Sensing

Mohamed-Amine Lahmeri, Walid R. Ghanem, Christina Bonfert, and Robert Schober

Abstract

In this paper, we investigate joint 3-dimensional (3D) trajectory planning and resource allocation for rotary-wing unmanned aerial vehicle (UAV) synthetic aperture radar (SAR) sensing. To support emerging real-time SAR applications and enable live mission control, we incorporate real-time communication with a ground station (GS). The UAV's main mission is the mapping of large areas of interest (AoIs) using an onboard SAR system and transferring the unprocessed raw radar data to the ground in real time. We propose a robust trajectory and resource allocation design that takes into account random UAV trajectory deviations. To this end, we model the UAV trajectory deviations and study their effect on the radar coverage. Then, we formulate a robust non-convex mixed-integer non-linear program (MINLP) such that the UAV 3D trajectory and resources are jointly optimized for maximization of the radar ground coverage. A low-complexity sub-optimal solution for the formulated problem is presented. Furthermore, to assess the performance of the sub-optimal algorithm, we derive an upper bound on the optimal solution based on monotonic optimization theory. Simulation results show that the proposed sub-optimal algorithm achieves close-to-optimal performance and not only outperforms several benchmark schemes but is also robust with respect to UAV trajectory deviations.

Index Terms

Optimization, communication, sensing, unmanned aerial vehicles, synthetic aperture radar, successive convex approximations, monotonic optimization.

Mohamed-Amine Lahmeri, Walid R. Ghanem, and Robert Schober are with the Institute for Digital Communications, Friedrich-Alexander University Erlangen-Nürnberg (FAU), Germany (emails: {amine.lahmeri, walid.ghanem, robert.schober}@fau.de). Christina Bonfert is with the Institute of Microwave Engineering, Ulm, Germany (email: christina.knill@uni-ulm.de). This paper was presented in part at the IEEE Global Communications Conference, Rio De Janeiro, Brazil, Dec. 2022 [1]. This work was supported in part by the Deutsche Forschungsgemeinschaft (DFG, German Research Foundation) GRK 2680 – Project-ID 437847244.

I. INTRODUCTION

Synthetic aperture radar (SAR) is a moving radar system that uses the flight path of a moving platform to simulate a large aperture [1], [2]. In classical radar systems, the spatial resolution depends on the ratio of the wavelength of the radar signal to the physical length of the antenna. This means that spatial resolution can be improved by using large antenna arrays, which are however often not practical. SAR overcomes this hurdle by using the motion of the moving platform to form a synthetic aperture where observations in different time slots, corresponding to different positions of the trajectory, are jointly processed to create the final image of the target area [3], [4]. SAR can provide high-resolution two-dimensional (2D) and even three-dimensional (3D) images [5], [6]. The benefits of SAR also include its resilience to harsh weather conditions and its ability to operate at day and night. In addition, SAR is non-invasive, which is useful for applications where penetration or direct contact with the area of interest (AoI) is not possible or not desirable, such as imaging of glaciers and wetlands [5]. Thanks to these features, SAR sensing has been employed in a variety of applications, such as environmental monitoring, agriculture, and surveillance.

SAR sensing has traditionally relied on airborne and spaceborne systems such as satellites and aircraft. However, these types of platforms lack flexibility and their revisit time for a given AoI is often large [2]. In this context, the recent growth of the drone industry has motivated the use of SAR onboard small and lightweight unmanned aerial vehicles (UAVs), which is promising and challenging at the same time. On the one hand, SAR sensing benefits from the high flexibility and the easy deployment of small drones at relatively short distances from AoIs. Consequently, UAV-based SAR sensing, which is now possible at low cost, facilitates short revisit times and enables various new applications, such as the monitoring of highly dynamic environments. On the other hand, the drones' limited hardware capacity is confronted with highly computationally complex SAR image processing algorithms [7]. This makes real-time SAR, which is an emerging SAR application [8], [9], difficult to realize onboard the flying platform. In this regard, one potential solution is to transmit the SAR raw data to the ground for processing, which requires a reliable communication link between the UAV and the ground [10]–[12]. In real-time SAR, the radar raw data received for each sensing pulse is processed with minimum delay such that the SAR image frame can be generated as a function of the received SAR raw data. This facilitates immediate adjustments based on the processed SAR data. Moreover, UAV instability presents

another challenge facing UAV-SAR systems. In fact, lightweight drones are vulnerable to external perturbations such as wind and atmospheric turbulence [13]. In this context, robust trajectory and resource allocation design with respect to (w.r.t.) UAV jittering were investigated for UAV-based communication systems [14], [15]. Another challenge is the drones' limited battery capacity [16]. Optimizing the UAV's energy consumption requires a careful trajectory design as energy consumption and SAR sensing performance are tightly coupled.

In general, trajectory design and resource allocation for UAVs have been exhaustively studied in the literature [17], [18] and different optimization techniques ranging from classical optimization [19] to learning-based methods [20], [21] have been used to tackle the problem. However, for the UAV-SAR use case, trajectory design and resource allocation have not been comprehensively addressed. In fact, existing experimental works on UAV-SAR systems only investigate the practical deployment of the SAR sensors onboard small drones and report results of experimental measurement campaigns with intuitive pre-planned flight paths with fixed velocity and altitude [22]–[24]. Furthermore, existing experimental research works do not account for real-time SAR applications and are limited to offline image processing without considering a potential wireless communication link to the ground. Among the few works targeting the optimization of UAV-SAR systems, the authors in [25] jointly optimized a focus measure for the SAR images and the estimation of the platform trajectory. However, while the estimation error of the actual trajectory was minimized based on a nominal trajectory, the trajectory itself was not optimized in [25], and communication with the ground was not considered. Furthermore, for a bistatic UAV-SAR system, the authors in [26] investigated trajectory optimization for a cellular-connected bistatic UAV-SAR system, where the AoI was illuminated by a ground base station, and the energy consumption was minimized. Yet, the proposed solution is limited to bistatic systems with a stationary ground transmitter and a moving receiver, making it inapplicable for active monostatic systems, where both transmitter and receiver are mounted on the same moving platform. The authors in [27], [28] investigated the use of a geosynchronous SAR system, where the AoI was illuminated by a satellite and echoes were collected by a passive sensing UAV. For instance, in [27], a multi-objective optimization problem for minimization of the distance traveled by the UAV-SAR was formulated and solved. However, the trajectory design of passive bistatic UAV-SAR systems is fundamentally different from that of active monostatic UAV-SAR systems.

In this paper, we investigate the joint 3D trajectory and resource allocation design for communication-assisted UAV-based SAR sensing. Different from other works, we focus on active monostatic

SAR sensing, where the UAV-SAR enables real-time SAR applications by transmitting the collected radar data instantaneously to the ground for processing. To this end, the UAV 3D trajectory and resources are jointly optimized to maximize the radar ground coverage under communication, radar, and energy constraints. Our main contributions are summarized as follows:

- The joint 3D trajectory and resource allocation algorithm design is formulated as a non-convex mixed-integer non-linear program (MINLP). Our problem formulation takes into account the constraints imposed by both the radar and communication subsystems.
- The unavoidable UAV trajectory deviations are modeled based on their statistics and their effect on the UAV-SAR ground radar coverage is unveiled.
- Exploiting successive convex approximation (SCA), we propose a low-complexity sub-optimal solution for the formulated problem, which is robust w.r.t. UAV trajectory deviations. Furthermore, based on monotonic optimization theory, we provide an upper bound on the optimal solution to assess the performance of the proposed sub-optimal algorithm.
- Our simulation results show that the proposed sub-optimal algorithm achieves close-to-optimal performance. In addition, we demonstrate the superiority of the proposed solution in terms of radar coverage compared to several benchmark schemes and confirm its robustness against random trajectory deviations.

We note that this article extends the corresponding conference version [1]. In [1], only a non-robust sub-optimal algorithm was provided, and random UAV trajectory deviations were not accounted for. Moreover, the gap between the sub-optimal scheme and the optimal solution was not assessed in [1].

The remainder of this article is organized as follows. In Section II, we present the system model for the considered UAV-SAR system. In Section III, we model random UAV trajectory deviations and propose a concept for robust trajectory design. In Section IV, we first formulate an optimization problem for the joint 3D trajectory and resource allocation design for UAV-SAR systems. Then, a robust sub-optimal solution and a corresponding upper bound are provided. In Section V, we evaluate the performance of the proposed scheme using the derived upper bound and other benchmark schemes. Finally, Section VI concludes the paper and provides some directions for future research.

Notations: In this paper, lower-case letters x refer to scalar numbers, boldface lower-case letters \mathbf{x} denote vectors, and boldface upper-case letters \mathbf{X} refer to matrices. $\{a, \dots, b\}$ denotes the set of all integers between a and b . $|\cdot|$ denotes the absolute value operator, whereas $\|\cdot\|_2$

refers to the L_2 -norm. Operators $[x]^+$ and $\lceil x \rceil$ correspond to $\max(0, x)$ and the ceiling function of x , respectively. For given sets \mathcal{X}_1 and \mathcal{X}_2 , $\mathcal{X}_1 \setminus \mathcal{X}_2$ is the set that comprises all elements of \mathcal{X}_1 that are not in \mathcal{X}_2 . \mathbb{N} represents the set of natural numbers. For arbitrary integer k , \mathbb{N}_k is the set $\{1, \dots, k\}$. $\mathbb{R}^{N \times 1}$ represents the set of $N \times 1$ vectors with real-valued entries, $\mathbb{R}_+^{N \times 1}$ denotes the set of $N \times 1$ vectors with non-negative real entries, and $\mathbb{R}^{N \times M}$ denotes the set of real $N \times M$ matrices. For $a, b \in \mathbb{N}$, $a \bmod b$ is the remainder of the division of a by b . For vector \mathbf{x} , vector \mathbf{x}^T stands for its transpose. For vectors $\mathbf{x} = [x(1), \dots, x(N)]^T \in \mathbb{R}^{N \times 1}$ and $\mathbf{y} = [y(1), \dots, y(N)]^T \in \mathbb{R}^{N \times 1}$, $\mathbf{x} \leq \mathbf{y}$ and $\mathbf{x} < \mathbf{y}$ define element-wise order relations on vectors \mathbf{x} and \mathbf{y} , i.e., $x(n) \leq y(n)$ and $x(n) < y(n)$, $\forall n$, respectively. For $\mathbf{A} \in \mathbb{R}^{N \times N}$, $\mathbf{A} \succeq \mathbf{0}$ indicates that \mathbf{A} is a positive semi-definite matrix. For a given random variable $X \in \mathbb{R}$, F_X denotes its cumulative distribution function (CDF) and $X \sim \mathcal{N}(\mu, \sigma)$ means that X is Gaussian distributed with mean μ and standard deviation σ . $\mathbb{P}(\cdot)$ denotes the probability operator. For a real-valued function $f(x)$, $f'(x)$ denotes the derivative of f . $\text{erf}(\cdot)$ is the Gaussian error function. In Table I, we introduce the definition of most important variables used in this paper.

TABLE I
DEFINITION OF MOST IMPORTANT VARIABLES.

Variable	Definition	Variable	Definition
L	Length of the AoI	$\text{SNR}_n(\mathbf{P}_{\text{sar}}, \mathbf{u})$	Instantaneous radar signal-to-noise ratio (SNR)
N	Number of azimuth sweeps	R_{sl}	Synchronization and localization data size
M	Number of time slots per azimuth scan	$R_{\text{min},n}(\mathbf{u})$	Instantaneous SAR data rate
z_{max} and z_{min}	UAV maximum and minimum altitudes	$R_n(\mathbf{P}_{\text{com}}, \mathbf{u})$	Instantaneous UAV data rate
$\mathbf{u}(n)$	UAV 3D location in time slot n	B_c	Communication bandwidth
$q(n)$	Remaining battery capacity in time slot n	γ	Reference channel power gain
$P_{\text{sar}}(n)$	Instantaneous SAR transmit power	\mathbf{g}	Ground station (GS) 3D location
$P_{\text{com}}(n)$	Instantaneous communication transmit power	$d_n(\mathbf{u})$	UAV-GS distance in time slot n
$P_{\text{sar}}^{\text{max}}$	Maximum SAR transmit power	v	UAV velocity
$P_{\text{com}}^{\text{max}}$	Maximum communication transmit power	q_{start}	Initial UAV battery capacity
\mathbf{P}_{sar}	SAR transmit power vector	P_{prop}	UAV propulsion power
\mathbf{P}_{com}	Communication transmit power vector	$E_n(\mathbf{P}_{\text{sar}}, \mathbf{P}_{\text{com}})$	Total energy consumed during time slot n
τ_p and PRF	Pulse duration and repetition frequency	$S_n(\mathbf{u})$	UAV SAR swath width in time slot n
θ_d and $\theta_{3\text{db}}$	Radar depression angle and beamwidth	$C(\mathbf{u})$	Total SAR ground coverage
B_r	Radar bandwidth	r	Coverage reliability level
f	Radar center frequency	$\delta_{\mathbf{p}_N}^r$	Near-range compensation vector
SNR_{min}	Minimum radar SNR	$\delta_{\mathbf{p}_F}^r$	Far-range compensation vector

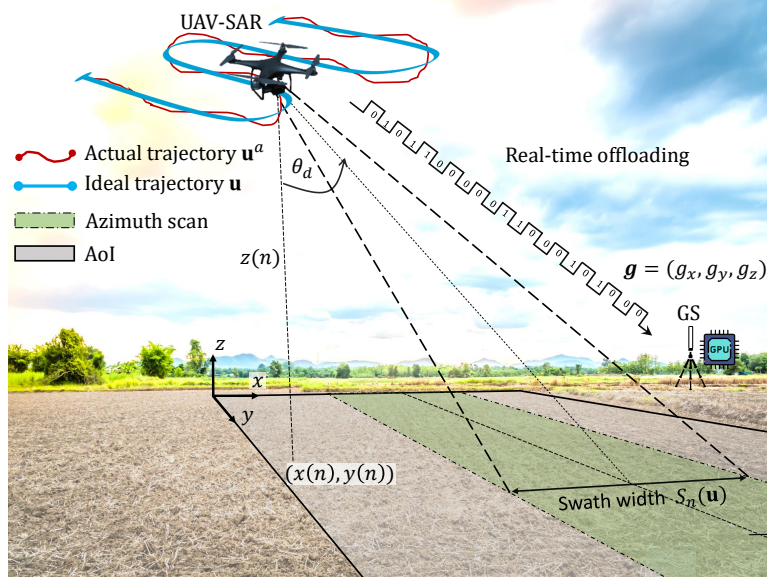


Fig. 1. System model for UAV-SAR system with real-time data offloading to a GS.

II. SYSTEM MODEL

We consider a rotary-wing UAV equipped with a side-looking radar system designed to perform SAR. The main mission of the UAV is to scan a certain AoI on the ground. To enable live mission control of the UAV-SAR system, real-time SAR processing is facilitated by transmitting the sensing data to a GS in real-time.

A. Trajectory Design

As a stripmap SAR mode [2] is employed, we assume that the AoI is rectangular with a given length L . Without loss of generality, we place the origin of the adopted coordinate system at the corner of the AoI, where the UAV mission starts, see Figure 1. To enable real-time processing of the SAR images, we assume that frequency-domain algorithms are employed due to their computational efficiency [4], [8], [9]. These algorithms impose the use of a linear UAV trajectory with fixed velocity $v > 0$ and zero acceleration [29]. The x -axis and y -axis define the range and azimuth direction, respectively, see Figure 1. We discretize time such that the length of the area scanned in y -direction in time slot n of duration δ_t , denoted by Δ_s , is given by:

$$\Delta_s = \delta_t v. \quad (1)$$

The UAV trajectory consists of N linear azimuth scans, where each scan corresponds to a traversal in the y -direction from one edge of the AoI (i.e., $y = 0$) to the other (i.e., $y = L$) and vice versa,

see Figure 1. Here, the use of a linear trajectory is imposed by the SAR stripmap mode [2]. In each azimuth scan, M uniform pulses are transmitted from the radar system¹, making the total number of time slots equal to NM . The drone location in time slot $n \in \mathbb{N}_{NM}$ is defined by $\mathbf{u}(n) = [x(n), y(n), z(n)]^T$, where $x(n)$ and $y(n)$ represent the position in the xy -plane, while $z(n)$ denotes the drone altitude. The UAV trajectory $\mathbf{u} = [\mathbf{u}(1), \dots, \mathbf{u}(NM)]$ is designed such that successive azimuth scans are ideally adjacent with no gaps in the coverage. At the end of each azimuth scan, the UAV makes its turns and moves to the appropriate x -position for the next scan as defined later in (4) and (5). The UAV altitude can be adjusted from scan to scan, but must be fixed during a given azimuth scan to have a fixed width of the on-ground footprint of the sensing beam along the range direction, i.e., fixed swath width. Consequently, the radar power is also adjusted from one azimuth scan to the next, such that the minimum required sensing SNR is achieved, but is fixed during a given scan. To account for these limitations of practical radar systems, we define two sets of time slots, denoted by \mathcal{A} and \mathcal{A}^c , as follows:

$$\mathcal{A} = \{k \in \mathbb{N}_{NM} | (k-1) \bmod M \neq 0\}, \quad (2)$$

$$\mathcal{A}^c = \mathbb{N}_{NM} \setminus \mathcal{A} = \{1 + (k-1)M, k \in \mathbb{N}_N\}. \quad (3)$$

Sets \mathcal{A} and \mathcal{A}^c will be used to (i) force a back-and-forth linear motion and (ii) set all of the relevant radar parameters, such as the radar power and altitude, constant during a given scan [23], [30]. To this end, set \mathcal{A}^c contains the N indices of the first time slots at the beginning of each azimuth scan, where the radar parameters can be adjusted, whereas set \mathcal{A} contains the indices of all other time slots, where the parameters are fixed. The following constraints on the drone trajectory are imposed:

$$\text{C1} : x(1) = -c_1 z(1), \quad (4)$$

$$\text{C2} : x(n) = x(n-1) + c_2 z(n-1) - c_1 z(n), \forall n \in \mathcal{A}^c \setminus \{1\}, \quad (5)$$

$$\text{C3} : x(n+1) = x(n), \forall n \in \mathcal{A}, \quad (6)$$

$$\text{C4} : z(n+1) = z(n), \forall n \in \mathcal{A}, \quad (7)$$

where $c_1 = \tan(\theta_1)$, $c_2 = \tan(\theta_2)$, $\theta_1 = \theta_d - \frac{\Theta_{3\text{dB}}}{2}$, $\theta_2 = \theta_d + \frac{\Theta_{3\text{dB}}}{2}$, $\Theta_{3\text{dB}}$ is the radar antenna 3dB beam width, and θ_d is the radar depression angle, see Figure 1. Constraint C2 ensures that two successive radar azimuth scans of the ground are adjacent without any gap between them.

¹Here, Δ_s is set such that $M\Delta_s = L$.

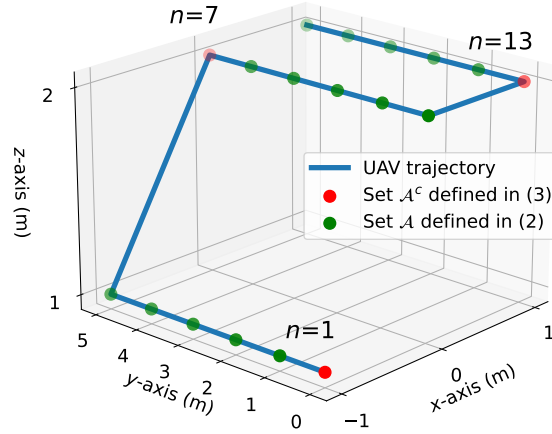


Fig. 2. Illustration of a Boustrophedon-shaped trajectory as imposed by constraints C1 – C4 for $N = 3$, $M = 6$, and a set of altitudes $\{1, 2, 2\}$ m.

During each scan, constraint C3 imposes a linear motion, while constraint C4 ensures a fixed altitude during a scan. In a nutshell, constraints C1 – C4 give rise to a Boustrophedon-shaped trajectory, as illustrated in Figure 2. Forcing a linear motion for stripmap UAV-SAR does not mean that the trajectory is completely fixed. In fact, in each turn, the drone’s z -position (altitude) and x -position can be adjusted. Only the y -position is fixed such that back-and-forth stripmap mode motion is guaranteed. The y -position is defined as follows:

$$y(1) = 0, \quad y(n) = y(n-1) + c(n-1)\Delta_s, \quad \forall n \in \mathbb{N}_{NM} \setminus \{1\}, \quad (8)$$

where vector $\mathbf{c} = [c(1), \dots, c(NM)]^T \in \mathbb{R}^{NM \times 1}$ is defined as follows:

$$\mathbf{c} = \underbrace{[1, \dots, 1]}_{M \text{ times}} \underbrace{[-1, \dots, -1, \dots]}_{M \text{ times}}^T. \quad (9)$$

B. Radar Imaging

Since we operate at relatively low altitudes, the maximal imageable area on the ground is limited by the antenna beam width. In time slot n , the width in x -direction of the on-ground footprint of the sensing beam, also referred to as SAR swath width, is denoted by S_n and given as follows:

$$S_n(\mathbf{u}) = (c_2 - c_1) z(n). \quad (10)$$

Following the trajectory \mathbf{u} , the total ground area covered by the drone is the sum of all infinitesimal small swath widths, and therefore can be approximated² as follows:

$$C(\mathbf{u}) = \sum_{n=1}^{NM} \Delta_s S_n(\mathbf{u}). \quad (11)$$

The data rate produced by the SAR sensing data in time slot n can be expressed as [31]:

$$R_{\min,n}(\mathbf{u}) = B_r \left(\frac{2 z(n) \Omega}{c} + \tau_p \right) \text{PRF}, \quad (12)$$

where B_r is the radar bandwidth, τ_p is the radar pulse duration, c is the speed of light, PRF is the radar pulse repetition frequency, and Ω is given by:

$$\Omega = \frac{\cos(\theta_1) - \cos(\theta_2)}{\cos(\theta_1) \cos(\theta_2)}. \quad (13)$$

Furthermore, the achieved radar SNR in time slot n is given as follows [32]:

$$\text{SNR}_n(\mathbf{P}_{\text{sar}}, \mathbf{u}) = \frac{P_{\text{sar}}(n) G_t G_r \lambda^3 \sigma_0 c \tau_p \text{PRF} \sin^2(\theta_d)}{(4\pi)^4 z^3(n) k_B T_o N F B_r L_{\text{tot}} v}, \quad (14)$$

where $\mathbf{P}_{\text{sar}} = [P_{\text{sar}}(1), \dots, P_{\text{sar}}(NM)]^T$, $P_{\text{sar}}(n)$ is the radar transmit power in time slot n , G_t and G_r are the radar antenna gains for transmission and reception, respectively, λ is the radar wavelength, σ_0 is the backscattering coefficient, k_B is Boltzmann's constant, T_o is the equivalent noise temperature, NF is the system noise figure, and L_{tot} represents the total radar losses.

C. UAV Data Link

We denote the location of the GS by $\mathbf{g} = [g_x, g_y, g_z]^T$. In time slot n , the distance between the drone and the GS is given by:

$$d_n(\mathbf{u}) = \sqrt{(x(n) - g_x)^2 + (y(n) - g_y)^2 + (z(n) - g_z)^2}. \quad (15)$$

We assume a line-of-sight (LOS) communication link to the GS. Thus, based on the free space path loss model³, the instantaneous throughput of the backhaul link between the UAV and the GS is given by:

$$R_n(\mathbf{P}_{\text{com}}, \mathbf{u}) = B_c \log_2 \left(1 + \frac{P_{\text{com}}(n) \gamma}{d_n^2(\mathbf{u})} \right), \quad (16)$$

²The approximation is due to the elliptical shape of the beam footprint on the ground and becomes negligible for large M .

³The offline optimization framework proposed in this paper can be extended to other communication channels with small-scale and large-scale fading components by an adequate design of the link margin that accounts for the channel power fluctuations [33].

where $\mathbf{P}_{\text{com}} = [P_{\text{com}}(1), \dots, P_{\text{com}}(NM)]^T$, $P_{\text{com}}(n)$ is the power allocated for communication in time slot n , B_c is the communication bandwidth, and γ is the channel power gain at a reference distance of 1 m divided by the noise variance. To guarantee successful real-time backhauling of the sensing data collected by the drone to the GS, the following inequality must be satisfied at all times:

$$R_n(\mathbf{P}_{\text{com}}, \mathbf{u}) \geq R_{\text{min},n}(\mathbf{u}) + R_{\text{sl}}, \forall n \in \mathbb{N}_{NM}, \quad (17)$$

where R_{sl} is the fixed data rate needed to transmit the synchronization and localization data necessary for successful radar image processing. In this work, we assume that the communication system operates in a licensed frequency band that is different from the one used for sensing, thus, avoiding interference that could lead to transmission failures. Lastly, the total energy consumed by the UAV in time slot n is given by:

$$E_n(\mathbf{P}_{\text{com}}, \mathbf{P}_{\text{sar}}) = \delta_t (\mathbf{P}_{\text{com}}(n) + \mathbf{P}_{\text{sar}}(n) + P_{\text{prop}}), \quad (18)$$

where P_{prop} is the propulsion power required for maintaining the operation of the drone and is given by [34]:

$$P_{\text{prop}} = P_0 \left(1 + \frac{3v^2}{U_{\text{tip}}^2} \right) + P_I \left(\sqrt{1 + \frac{v^4}{4v_0^4} - \frac{v^2}{2v_0^2}} \right)^{\frac{1}{2}} + \frac{1}{2} d_0 \rho s A v^3. \quad (19)$$

Here, P_0 and P_I are two constants defined in [34], U_{tip} is the tip speed of the rotor blade, d_0 is the fuselage drag ratio, ρ is the air density, s is the rotor solidity, A is the rotor disc area, $v_0 = \sqrt{\frac{W_u}{2\rho A}}$ is the mean rotor induced velocity in hover, and W_u is the UAV weight in Newton. Note that, in this work, the propulsion power is constant since the drone's velocity, v , is fixed to allow for efficient signal processing of the SAR images.

III. ROBUST UAV TRAJECTORY DESIGN UNDER RANDOM POSITION DEVIATIONS

In practice, it is difficult for lightweight drones to strictly follow a designed trajectory due to perturbations caused by weather conditions, mechanical vibrations, and localization errors [13]. These errors may result in areas not covered by SAR. In this section, we first develop a model for UAV trajectory deviations and quantify their impact on the footprint of the sensing beam. Then, we propose a statistics-based robust trajectory design that suitably widens and adjusts the sensing beam footprint. This creates overlapping scans and allows covering the AoI without gaps.

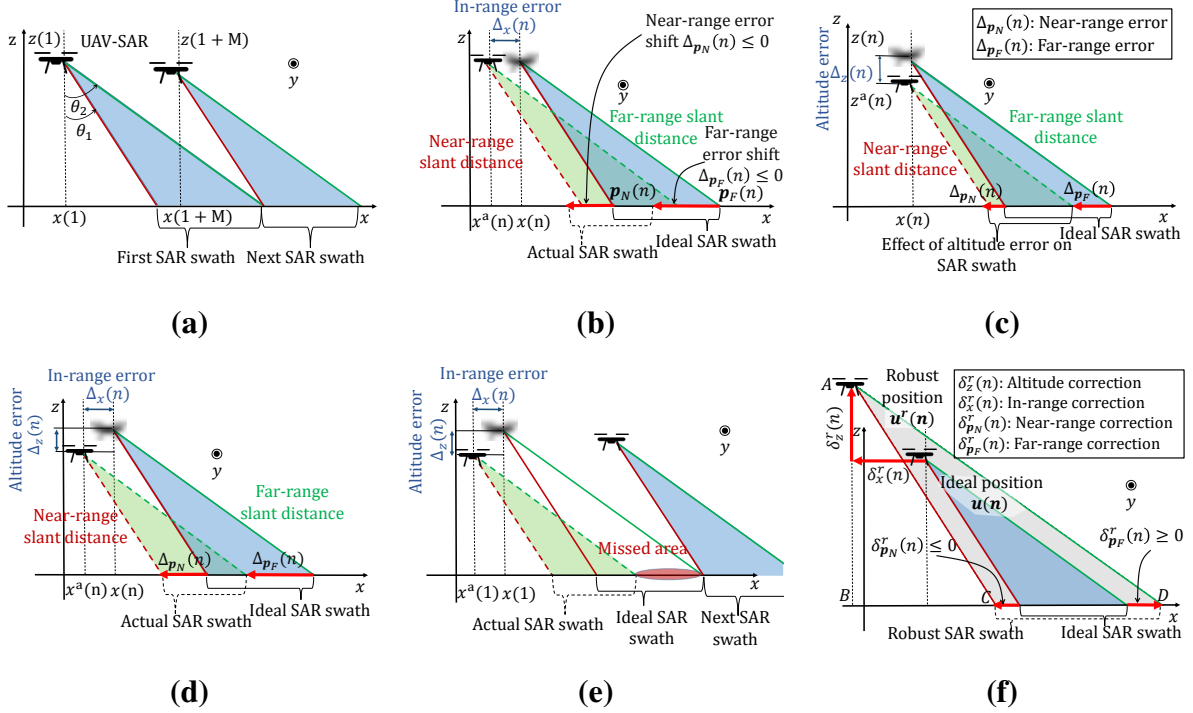


Fig. 3. Robust UAV trajectory design. (a) Successive azimuth scans for an ideal trajectory. (b) Effect of in-range error on the ground SAR swath. (c) Effect of altitude error on the ground SAR swath. (d) Combined effect of in-range and altitude errors on the ground SAR swath. (e) Uncovered areas due to UAV flight deviations. (f) Proposed robust UAV-SAR trajectory.

A. Trajectory Deviation Model

If the actual trajectory is different from the ideal linear trajectory \mathbf{u} , described by C1 – C4, the actual footprint of the sensing beam is also affected in terms of both its on-ground position and width. Let position vectors $(\mathbf{x}^a, \mathbf{y}^a, \mathbf{z}^a) \in \mathbb{R}^{NM \times 1}$ describe the actual trajectory, denoted by $\mathbf{u}^a = [\mathbf{u}^a(1), \dots, \mathbf{u}^a(NM)]$, where the drone's actual position in time slot n is given by $\mathbf{u}^a(n) = [x^a(n), y^a(n), z^a(n)]^T$. In what follows, we quantify the change in the actual footprint of the sensing beam due to random UAV trajectory deviations.

1) *Cross-range error*: The deviation in y -direction, denoted by $\Delta_y = \mathbf{y}^a - \mathbf{y} = [\Delta_y(1), \dots, \Delta_y(NM)]^T \in \mathbb{R}^{NM \times 1}$, has the least effect on the SAR ground coverage. Although this error can affect the SAR resolution by influencing the illumination time of a given reference point on the ground, it has no effect on the radar coverage thanks to the radar beam width in y -direction. In fact, the main idea behind SAR systems is to use this direction to create the synthetic aperture such that any reference point on the ground is illuminated multiple times from different angles along the y -axis [2]. Therefore, in what follows, we neglect the effect of this

error on the radar coverage and focus on UAV trajectory deviations in the xz -plane.

2) *In-range error*: This error is caused by the UAV position deviation in x -direction and is denoted by vector $\Delta_x = \mathbf{x}^a - \mathbf{x} = [\Delta_x(1), \dots, \Delta_x(NM)]^T \in \mathbb{R}^{NM \times 1}$, see Figure 3b. As shown in the figure, this error causes near-range and far-range shifts of the ground footprint of the sensing beam along the x -axis. To this end, in the xz -plane and in time slot n , we define point $\mathbf{p}_N(n) = [x(n) + c_1 z(n), y(n), 0]^T$ representing the intersection between the near-range slant distance line and the x -axis and point $\mathbf{p}_F(n) = [x(n) + c_2 z(n), y(n), 0]^T$ representing the intersection between the far-range slant distance line and the x -axis. Both points are defined w.r.t. the drone's ideal trajectory, see Figure 3b. Any deviation from the ideal UAV position in the xz -plane results in a near-range error (shift of point $\mathbf{p}_N(n)$ along the x -axis), denoted by $\Delta_{\mathbf{p}_N} = [\Delta_{\mathbf{p}_N}(1), \dots, \Delta_{\mathbf{p}_N}(NM)]^T \in \mathbb{R}^{NM \times 1}$, and a far-range error (shift of point $\mathbf{p}_F(n)$ along the x -axis), denoted by $\Delta_{\mathbf{p}_F} = [\Delta_{\mathbf{p}_F}(1), \dots, \Delta_{\mathbf{p}_F}(NM)]^T \in \mathbb{R}^{NM \times 1}$, of the sensing beam footprint. A deviation in x -direction, causes identical near-range and far-range errors such that, in time slot n , $\Delta_{\mathbf{p}_F}(n) = \Delta_{\mathbf{p}_N}(n) = \Delta_x(n)$. Therefore, an in-range error does not affect the width of the SAR swath, but results in a translation of the footprint of the sensing beam along the x -axis as shown in Figure 3b.

3) *Altitude error*: A deviation of the trajectory in z -direction, given by $\Delta_z = \mathbf{z}^a - \mathbf{z} = [\Delta_z(1), \dots, \Delta_z(NM)]^T \in \mathbb{R}^{NM \times 1}$, results in non-equal far-range and near-range errors. In fact, an altitude error in time slot n , denoted by $\Delta_z(n)$, results in $\Delta_{\mathbf{p}_N}(n) = c_1 \Delta_z(n)$ and $\Delta_{\mathbf{p}_F}(n) = c_2 \Delta_z(n)$. In contrast to in-range errors, altitude errors induce a change in both the width and the position of the sensing beam footprint, see Figure 3c.

As shown in Figure 3d, in time slot n , the combined in-range and altitude errors result in a near-range error of the footprint of the sensing beam given by:

$$\Delta_{\mathbf{p}_N}(n) = \Delta_x(n) + c_1 \Delta_z(n). \quad (20)$$

Similarly, in time slot n , the total far-range error is given by:

$$\Delta_{\mathbf{p}_F}(n) = \Delta_x(n) + c_2 \Delta_z(n). \quad (21)$$

4) *Trajectory deviation model*: In this work, based on measurements in [35], [36], we propose to model the UAV-SAR trajectory deviations as independent Gaussian random variables such that, in each time slot n , $\Delta_x(n) \sim \mathcal{N}(o_x, \sigma)$ and $\Delta_z(n) \sim \mathcal{N}(o_z, \sigma)$, $\forall n$. The standard deviation, denoted by σ , depends on the stability of the UAV in the presence of external perturbations

caused, e.g., by adverse weather conditions. The offsets in x - and z -direction, denoted by o_x and o_z , respectively, represent a possible constant error between the UAV's actual trajectory and its ideal intended trajectory and depend on the UAV localization accuracy. For the special case, $o_x = o_z = 0$, the UAV trajectory deviations reduce to random fluctuations around the ideal trajectory, also referred to as UAV jittering [14].

B. Proposed Robust Trajectory Design

Both positive near-range errors, i.e., $\Delta_{\mathbf{p}_N}(n) > 0$, and negative far-range errors, i.e., $\Delta_{\mathbf{p}_F}(n) < 0$, result in uncovered areas, whereas the reverse result in an overlap between successive scans, see Figure 3e. For robust trajectory design, uncovered areas are avoided by tolerating an overlap between adjacent azimuth scans. This can be achieved by shifting the actual footprint of the sensing beam such that the near-range and far-range errors are compensated. Since excessive overlap between scans reduces the SAR coverage, the overlap should be limited to the degree needed for compensation of UAV trajectory deviations. To this end, we define the coverage reliability level r , $0 \leq r \leq 1$, as the probability of having no gaps between successive SAR azimuth scans. The compensation that is required in the near range of the sensing beam footprint to achieve coverage reliability level r is denoted by $\delta_{\mathbf{p}_N}^r = [\delta_{\mathbf{p}_N}^r(1), \dots, \delta_{\mathbf{p}_N}^r(NM)]^T \in \mathbb{R}^{NM \times 1}$, and is obtained as:

$$\delta_{\mathbf{p}_N}^r(n) = \arg \min_s \left\{ |s| \mid s \in \mathbb{R}, \mathbb{P}(\Delta_{\mathbf{p}_N}(n) + s \leq 0) \geq r \right\}. \quad (22)$$

Similarly, the far-range compensation, which we denote by $\delta_{\mathbf{p}_F}^r = [\delta_{\mathbf{p}_F}^r(1), \dots, \delta_{\mathbf{p}_F}^r(NM)]^T \in \mathbb{R}^{NM \times 1}$, is obtained as:

$$\delta_{\mathbf{p}_F}^r(n) = \arg \min_s \left\{ |s| \mid s \in \mathbb{R}, \mathbb{P}(\Delta_{\mathbf{p}_F}(n) + s \geq 0) \geq r \right\}. \quad (23)$$

Note that, on the one hand, to avoid coverage holes, coverage reliability values close to 1 are desirable. On the other hand, if r is chosen too close to 1, this might result in a reduction of the total coverage, as a larger swath overlap is required to compensate for random trajectory deviations. Based on our simulations, $r = 0.95$ provides a good compromise between coverage reliability and total coverage.

Next, given the trajectory deviation statistics, we derive analytical expressions for the near-range and far-range compensations.

Proposition 1. *The near-range and far-range compensations given in (22) and (23), respectively, can be obtained in time slot n as follows:*

$$\delta_{\mathbf{p}_N}^r(n) = -\left[\text{erf}^{-1}(2r-1)\sigma\sqrt{2(1+c_1^2)} + o_x + c_1o_z\right]^+, \quad (24)$$

$$\delta_{\mathbf{p}_F}^r(n) = \left[\text{erf}^{-1}(2r-1)\sigma\sqrt{2(1+c_2^2)} - o_x - c_2o_z\right]^+. \quad (25)$$

Proof. Please refer to Appendix A. □

Remark 1. Note that $\delta_{\mathbf{p}_N}^r(n) \leq 0$, whereas $\delta_{\mathbf{p}_F}^r(n) \geq 0$, $\forall n \in \mathbb{N}_{NM}$, which means that the actual footprint of the radar beam is widened, see Figure 3f. This creates overlapping scans that prevent gaps between adjacent scans.

The proposed near-range and far-range compensations can be used to adjust the UAV position. In the following proposition, we translate the near-range and far-range compensation of the beam footprint to an in-range (x -position) adjustment, denoted by $\boldsymbol{\delta}_x^r = [\delta_x^r(1), \dots, \delta_x^r(NM)]^T \in \mathbb{R}^{NM \times 1}$, and an altitude (z -position) adjustment, denoted by $\boldsymbol{\delta}_z^r = [\delta_z^r(1), \dots, \delta_z^r(NM)]^T \in \mathbb{R}^{NM \times 1}$, as shown in Figure 3f.

Proposition 2. *Given the near-range and far-range compensation of the beam footprint, $\boldsymbol{\delta}_{\mathbf{p}_N}^r$ and $\boldsymbol{\delta}_{\mathbf{p}_F}^r$, the corresponding in-range and altitude adjustment of the UAV position are respectively given by:*

$$\boldsymbol{\delta}_x^r = \boldsymbol{\delta}_{\mathbf{p}_N}^r - c_1 \boldsymbol{\delta}_z^r, \quad (26)$$

$$\boldsymbol{\delta}_z^r = \frac{\boldsymbol{\delta}_{\mathbf{p}_F}^r - \boldsymbol{\delta}_{\mathbf{p}_N}^r}{c_2 - c_1}. \quad (27)$$

Proof. Based on the geometry of the problem, In time slot n , given $\delta_{\mathbf{p}_N}^r(n) \leq 0$ and $\delta_{\mathbf{p}_F}^r(n) \geq 0$, we shift the UAV position along the x -axis by $\delta_x^r(n) \leq 0$, and along the z -axis by $\delta_z^r(n) \geq 0$, see Figure 3f. The required UAV position adjustments can be derived based on the geometry of the problem by solving the following system of equations:

$$\begin{cases} c_1 = \frac{c_1 z(n) + \delta_{\mathbf{p}_N}^r(n) - \delta_x^r(n)}{z(n) + \delta_z^r(n)}, \\ c_2 = \frac{c_2 z(n) + \delta_{\mathbf{p}_F}^r(n) - \delta_x^r(n)}{z(n) + \delta_z^r(n)}, \end{cases} \quad (28)$$

where the first and second lines of (28) are obtained from triangles (ABC) and (ABD) in Figure 3f, respectively. □

For robust UAV-SAR trajectory design, the UAV position is adjusted in each time slot to achieve a coverage reliability level r in the presence of UAV trajectory deviations. Consequently,

the robust trajectory is denoted by $\mathbf{u}^r = [\mathbf{u}^r(1), \dots, \mathbf{u}^r(NM)]$, where $\mathbf{u}^r(n)$ is the adjusted position in time slot n and is given by:

$$\mathbf{u}^r(n) = [x^r(n), y(n), z^r(n)]^T = [x(n) + \delta_x^r(n), y(n), z(n) + \delta_z^r(n)]^T. \quad (29)$$

IV. ROBUST RESOURCE ALLOCATION AND TRAJECTORY OPTIMIZATION FRAMEWORK

In this section, we formulate an optimization problem for joint 3D trajectory and resource allocation design. The formulated problem is solved offline where random UAV trajectory deviations are accounted for via the robust trajectory given in (29). In particular, for a given coverage reliability level r , we provide a low-complexity sub-optimal solution of the formulated problem based on SCA. Moreover, to assess the performance of the proposed sub-optimal scheme, we derive an upper bound for the optimal solution based on monotonic optimization theory [41].

A. Problem Formulation

Our objective is the maximization of the drone ground coverage C while satisfying the constraints imposed by the radar and communication subsystems. We assume Gaussian trajectory deviation as described in Section III-A. To achieve a coverage reliability level r , the UAV follows the robust trajectory \mathbf{u}^r provided in (29). We optimize the drone trajectory $\{\mathbf{z}, \mathbf{x}, N\}$ and the power allocation $\{\mathbf{q}, \mathbf{P}_{\text{com}}, \mathbf{P}_{\text{sar}}\}$, where vectors \mathbf{z} , \mathbf{x} , \mathbf{q} , \mathbf{P}_{com} , and \mathbf{P}_{sar} , represent the collections of all $z(n)$, $x(n)$, $q(n)$, $P_{\text{com}}(n)$, and $P_{\text{sar}}(n)$, $\forall n \in \mathbb{N}_{NM}$, respectively, and $q(n)$ is the energy remaining in the drone's battery in time slot n . To this end, the following optimization problem is formulated:

$$\begin{aligned} \text{(P.1)} : \quad & \max_{\mathbf{z}, \mathbf{x}, \mathbf{q}, \mathbf{P}_{\text{sar}}, \mathbf{P}_{\text{com}}, N} C(\mathbf{u}^r) \\ \text{s.t.} \quad & \text{C1} - \text{C4}, \\ & \text{C5} : P_{\text{sar}}(n+1) = P_{\text{sar}}(n), \forall n \in \mathcal{A}, \\ & \text{C6} : z_{\min} \leq z^r(n) \leq z_{\max}, \forall n \in \mathbb{N}_{NM}, \\ & \text{C7} : \text{SNR}_n(\mathbf{P}_{\text{sar}}, \mathbf{u}^r) \geq \text{SNR}_{\min}, \forall n \in \mathbb{N}_{NM}, \\ & \text{C8} : R_n(\mathbf{P}_{\text{com}}, \mathbf{u}^r) \geq R_{\min, n}(\mathbf{u}^r) + R_{\text{sl}}, \forall n \in \mathbb{N}_{NM}, \\ & \text{C9} : 0 \leq P_{\text{sar}}(n) \leq P_{\text{sar}}^{\max}, 0 \leq P_{\text{com}}(n) \leq P_{\text{com}}^{\max}, \forall n \in \mathbb{N}_{NM}, \end{aligned}$$

$$\text{C10} : q(1) = q_{\text{start}}, q(n) \geq 0, \forall n \in \mathbb{N}_{NM},$$

$$\text{C11} : q(n+1) = q(n) - E_n(\mathbf{P}_{\text{sar}}, \mathbf{P}_{\text{com}}), \forall n \in \mathbb{N}_{NM-1},$$

$$\text{C12} : N \in \mathbb{N}.$$

Constraints C1 – C4 define the shape of the UAV ideal trajectory as described in (4)-(7). Constraint C5 ensures constant radar power along each azimuth scan. Constraint C6 determines the allowed range for the UAV's operational altitude when the drone follows the proposed robust trajectory. Constraint C7 ensures the minimum SNR, SNR_{min} , required for SAR imaging when the drone follows the robust trajectory \mathbf{u}^r given by (29). Constraint C8 guarantees successful real-time transmission of the SAR data collected by the UAV to the GS. Constraint C9 ensures that the radar and communication transmit powers are non-negative and do not exceed the maximum permissible levels. Constraint C10 specifies the energy available in the UAV battery, q_{start} , at the start of the mission, and ensures that the energy remaining in the battery during operation, $q(n)$, does not become negative. In addition, constraint C11 updates the UAV battery level in time slot $n+1$ by subtracting the total energy consumed during time slot n , denoted by $E_n(\mathbf{P}_{\text{sar}}, \mathbf{P}_{\text{com}})$, from $q(n)$. Constraint C12 defines the number of azimuth scans realized by the UAV which is an integer.

Problem (P.1) is a non-convex MINLP due to non-convex constraint C8 and integer variable constraint C12. The latter does not only affect the objective function but also the dimension of all other optimization variables. Therefore, N cannot be optimized jointly with the remaining variables. Furthermore, non-convex MINLPs are usually very difficult to solve. Nevertheless, in the following, we provide a low-complexity sub-optimal solution to problem (P.1) based on SCA.

B. Low-complexity Sub-optimal Solution of Problem (P.1)

In this subsection, we provide a low-complexity sub-optimal solution to problem (P.1) based on successive convex approximation (SCA). First, we fix the number of azimuth scans N and denote the resulting problem by (P.2):

$$\begin{aligned} \text{(P.2)} : \quad & \max_{\mathbf{z}, \mathbf{x}, \mathbf{q}, \mathbf{P}_{\text{sar}}, \mathbf{P}_{\text{com}}} C(\mathbf{u}^r) \\ \text{s.t.} \quad & \text{C1} - \text{C11}. \end{aligned}$$

However, even for a given N , problem (P.2) is still non-convex and difficult to solve. Thus, we approximate problem (P.2) as a convex problem and use iterative SCA to solve it. Then, we perform a search for the optimal number of azimuth scans N^* . As a first step, we transform constraint C7, which involves a cubic function of drone altitude z , using second-order cone programming. To this end, we introduce slack variables $\psi(n)$ stacked in vector $\boldsymbol{\psi} = [\psi(1), \dots, \psi(NM)]^T \in \mathbb{R}^{NM \times 1}$, and reformulate C7 as follows:

$$\text{C7a} : \begin{bmatrix} \psi(n) & z^r(n) \\ z^r(n) & 1 \end{bmatrix} \succeq \mathbf{0}, \forall n \in \mathbb{N}_{NM}, \quad (30)$$

$$\text{C7b} : \begin{bmatrix} P_{\text{sar}}(n)\beta & \psi(n) \\ \psi(n) & z^r(n) \end{bmatrix} \succeq \mathbf{0}, \forall n \in \mathbb{N}_{NM}, \quad (31)$$

$$\text{C7c} : \psi(n) \geq 0, \forall n \in \mathbb{N}_{NM}, \quad (32)$$

where $\beta = \frac{G_t G_r \lambda^3 \sigma_0 c \tau_p \text{PRF} \sin^2(\theta_d)}{(4\pi)^4 k_B T_o N F B_r L_{\text{tot}} v \text{SNR}_{\text{min}}}$. Furthermore, non-convex constraint C8 can be rewritten as follows:

$$\text{C8} : (A2^{\alpha z^r(n)} - 1) d_n^2(\mathbf{u}^r) \leq P_{\text{com}}(n)\gamma, \forall n \in \mathbb{N}_{NM}, \quad (33)$$

where $A = 2^{\frac{B_r \tau_p \text{PRF}}{B_c}}$ and $\alpha = \frac{2\Omega B_r \text{PRF}}{c B_c}$. In time slot n , let function $H_n(\mathbf{u}^r)$ be equal to the left-hand side of (33). Function H_n is non-convex w.r.t. to optimization variables x and z . Therefore, in each SCA iteration $j \in \mathbb{N}$, we use a Taylor series approximation around points $\{z^{(j)}(n), x^{(j)}(n)\} \in \mathbb{R}$ to convexify constraint C8. This is achieved by replacing function H_n with a global overestimate, denoted by \overline{H}_n . To this end, in time slot n , we first expand function H_n as follows:

$$H_n(\mathbf{u}^r) = h_1(z(n))h_2(z(n)) + h_1(z(n))h_3(x(n)) + h_1(z(n))(y(n) - g_y)^2, \quad (34)$$

where functions h_1, h_2 , and h_3 are convex differentiable functions that are given by:

$$h_1(z(n)) = A2^{\alpha z^r(n)} - 1, \quad (35)$$

$$h_2(z(n)) = (z^r(n) - g_z)^2, \quad (36)$$

$$h_3(x(n)) = (x^r(n) - g_x)^2. \quad (37)$$

Yet, terms $h_1(z(n))h_2(z(n))$ and $h_1(z(n))h_3(x(n))$ contain coupling and are non-convex w.r.t. optimization variables x and z . To overcome this obstacle, we rewrite them as follows:

$$h_1(z(n))h_2(z(n)) = \frac{1}{2}(h_1(z(n)) + h_2(z(n)))^2 - \frac{1}{2}h_1^2(z(n)) - \frac{1}{2}h_2^2(z(n)), \quad (38)$$

$$h_1(z(n))h_3(x(n)) = \frac{1}{2}(h_1(z(n)) + h_3(x(n)))^2 - \frac{1}{2}h_1^2(z(n)) - \frac{1}{2}h_3^2(x(n)). \quad (39)$$

Equations (38) and (39) are differences of convex functions, where functions $f_i = \frac{1}{2}h_i^2, i \in \{1, 2, 3\}$, represent an obstacle to solving problem (P.2). Therefore, we replace them with their global underestimates around points $\{z^{(j)}(n), x^{(j)}(n)\}$ based on Taylor series approximation:

$$\underline{f}_i(z(n)) = f_i(z^{(j)}(n)) + f'_i(z^{(j)}(n))(z(n) - z^{(j)}(n)), \forall i \in \{1, 2\}, \quad (40)$$

$$\underline{f}_3(x(n)) = f_3(x^{(j)}(n)) + f'_3(x^{(j)}(n))(x(n) - x^{(j)}(n)), \forall n. \quad (41)$$

Consequently, the global overestimate for function \overline{H}_n around $\{z^{(j)}(n), x^{(j)}(n)\}$ is given by:

$$\begin{aligned} \overline{H}_n(\mathbf{u}^r) = & \frac{1}{2}(h_1(z(n)) + h_2(z(n)))^2 + \frac{1}{2}(h_1(z(n)) + h_3(x(n)))^2 - \\ & 2\underline{f}_1(z(n)) - \underline{f}_2(z(n)) - \underline{f}_3(x(n)) + h_1(z(n))(y(n) - g_y)^2, \forall n. \end{aligned} \quad (42)$$

In the final step, we introduce two new slack vectors $\mathbf{t} = [t(1), \dots, t(NM)]^T \in \mathbb{R}^{NM \times 1}$, $\mathbf{o} = [o(1), \dots, o(NM)]^T \in \mathbb{R}^{NM \times 1}$, and two new constraints $\widetilde{\text{C8a}}$ and $\widetilde{\text{C8b}}$ to reformulate constraint C8 as follows:

$$\begin{aligned} \widetilde{\text{C8}} : & \frac{1}{2}t^2(n) + \frac{1}{2}o^2(n) - 2\underline{f}_1(z(n)) - \underline{f}_2(z(n)) - \underline{f}_3(x(n)) + \\ & h_1(z(n))(y(n) - g_y)^2 \leq P_{\text{com}}(n)\gamma, \forall n \in \mathbb{N}_{NM}, \end{aligned} \quad (43)$$

$$\widetilde{\text{C8a}} : h_1(z(n)) + h_2(z(n)) \leq t(n), \forall n \in \mathbb{N}_{NM}, \quad (44)$$

$$\widetilde{\text{C8b}} : h_1(z(n)) + h_3(z(n)) \leq o(n), \forall n \in \mathbb{N}_{NM}. \quad (45)$$

Let $\mathbf{z}^{(j)} \in \mathbb{R}^{NM \times 1}$ and $\mathbf{x}^{(j)} \in \mathbb{R}^{NM \times 1}$ be the collections of all $z(n)$ and $x(n), \forall n$, respectively. Problem (P.2) can be approximated around the solution $\{\mathbf{z}^{(j)}, \mathbf{x}^{(j)}\}$ by the following convex optimization problem:

$$\begin{aligned} \text{(P.3)} : & \max_{\mathbf{z}, \mathbf{x}, \mathbf{q}, \mathbf{P}_{\text{sar}}, \mathbf{P}_{\text{com}}, \psi, \mathbf{t}, \mathbf{o}} C(\mathbf{u}^r) \\ \text{s.t.} & \text{ C1} - \text{C6}, \text{C7a}, \text{C7b}, \text{C7c}, \widetilde{\text{C8}}, \widetilde{\text{C8a}}, \widetilde{\text{C8b}}, \text{C9} - \text{C11}. \end{aligned}$$

To solve (P.2), we use SCA such that in each iteration j of **Algorithm 1**, we update the solution $\{\mathbf{z}^{(j)}, \mathbf{x}^{(j)}\}$ by solving problem (P.3) using conventional solvers such as CVX [37]. To solve problem (P.1), we first solve problem (P.2) for every fixed and feasible number of drone scans N , then we select the minimum number of azimuth scans that results in the maximum coverage to save drone energy. In the following proposition, we show that the number of feasible

Algorithm 1 Successive Convex Approximation (SCA)

- 1: Initialization: Set iteration index $j = 1$, point $\{\mathbf{z}^{(1)}, \mathbf{x}^{(1)}\}$, coverage $C^{(1)}$ by solving (P.3) around point $\{\mathbf{z}^{(1)}, \mathbf{x}^{(1)}\}$, and error tolerance $0 < \epsilon \ll 1$.
 - 2: **repeat**
 - 3: Set $j = j + 1$ ▷ Increment iteration index
 - 4: Get coverage $C^{(j)}$ and solution $\{\mathbf{z}, \mathbf{x}, \mathbf{q}, \mathbf{P}_{\text{sar}}, \mathbf{P}_{\text{com}}\}$ by solving (P.3) around point $\{\mathbf{z}^{(j-1)}, \mathbf{x}^{(j-1)}\}$
 - 5: Set $\mathbf{z}^{(j)} = \mathbf{z}, \mathbf{x}^{(j)} = \mathbf{x}$ ▷ Update solution
 - 6: **until** $\left| \frac{C^{(j)} - C^{(j-1)}}{C^{(j)}} \right| \leq \epsilon$ ▷ Verify convergence
 - 7: **return** solution $\{\mathbf{z}^r, \mathbf{x}^r, \mathbf{q}, \mathbf{P}_{\text{sar}}, \mathbf{P}_{\text{com}}\}$
-

N is finite, and therefore, the exhaustive search is guaranteed to yield the optimal number of azimuth scans N .

Proposition 3. *The feasible number of azimuth scans N is finite. The optimal number of azimuth scans N^* is upper bounded by $\frac{1}{M} \left(\frac{q_{\text{start}}}{\delta_t P_{\text{prop}}} + 1 \right)$.*

Proof: Please refer to Appendix B. ■

Algorithm 1 has a polynomial time complexity [38]. The exhaustive search is of constant time complexity as the total number of iterations is less than $\left\lceil \frac{1}{M} \left(\frac{q_{\text{start}}}{\delta_t P_{\text{prop}}} + 1 \right) \right\rceil$ according to **Proposition 3**. Therefore, the overall time complexity of the proposed robust scheme is still polynomial. Moreover, **Algorithm 1** converges to a local optimum of problem (P.1) as SCA methods are known to converge fast to locally optimal solutions [39]. Next, to assess the performance of the proposed robust sub-optimal scheme, we derive an upper bound on the optimal solution of problem (P.1) using monotonic optimization theory [40].

C. Upper Bound on the Optimal Solution of Problem (P.1)

To provide an upper bound to problem (P.1), we start by fixing the total number of azimuth scans N , which leads to problem (P.2). However, problem (P.2) is non-monotonic w.r.t. optimization variables \mathbf{x} , \mathbf{z} , and \mathbf{P}_{com} , due to constraints C2 and C8. Equality constraints C3 – C5 also represent an obstacle to applying monotonic optimization theory. In what follows, we provide an upper bound on the optimal solution to problem (P.2). To this end, we introduce an optimization problem, denoted by $(\overline{\text{P.2}})$, the optimal solution of which presents an upper

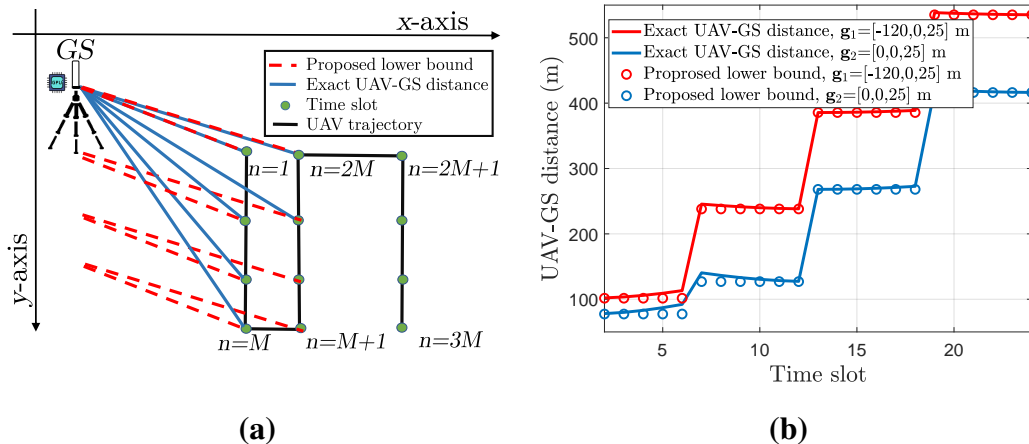


Fig. 4. Lower bound on the UAV-GS distance. (a) Proposed lower bound. (b) Accuracy of the proposed lower bound.

bound on the optimal solution to problem (P.2). Then, we use monotonic optimization theory to provide the optimal solution to problem $(\overline{\text{P.2}})$.

1) *Upper Bound Formulation:* During the M time slots of a given azimuth scan, the UAV-GS distance slightly varies depending on the AoI-GS distance. In each azimuth scan, we impose an upper bound on the UAV throughput R_n by lower-bounding the UAV-GS distance d_n . In fact, for a given azimuth scan, we consider the minimum possible UAV-GS distance in the considered scan, see Figure 4a. Following the proposed lower-bound, the UAV-GS distance is constant during a scan and only varies from scan to scan. This approach allows us to focus on optimizing the system parameters from scan to scan, instead of optimizing the system along all time slots, which reduces the problem dimension from $N \times M$ to N . Hereinafter, each $n \in \mathbb{N}_N$, refers to the start of a different azimuth scan. The y -positions that correspond to the minimum UAV-GS distance for each azimuth scan, denoted by $\overline{\mathbf{y}} = [\overline{y}(1), \dots, \overline{y}(N)]^T \in \mathbb{R}^{N \times 1}$, are given by:

$$\overline{y}(n) = y(i), i = \arg \min_{1+(n-1)M \leq k \leq nM} (y(k) - g_y)^2. \quad (47)$$

In Figure 4b, we plot the exact UAV-GS distance with solid lines and the proposed lower bound on the UAV-GS distance with circle markers. The figure confirms the tightness of the proposed lower bound for different placements of the GS. The parameter values used in Figure 4b are specified in Table II. As each time slot now corresponds to a different azimuth scan, we define vectors $\overline{\delta}_x^r$ and $\overline{\delta}_z^r$ that contain the corrections in x - and z -direction, respectively, for each of

these scans as follows:

$$\overline{\boldsymbol{\delta}}_x^r = [\delta_x^r(1), \delta_x^r(1 + M), \dots, \delta_x^r(1 + (N - 1)M)]^T \in \mathbb{R}^{N \times 1}, \quad (48)$$

$$\overline{\boldsymbol{\delta}}_z^r = [\delta_z^r(1), \delta_z^r(1 + M), \dots, \delta_z^r(1 + (N - 1)M)]^T \in \mathbb{R}^{N \times 1}, \quad (49)$$

Based on this approach, the following N -dimensional optimization problem denoted by $(\overline{\text{P.2}})$ is obtained as an upper bound for optimization problem (P.2):

$$(\overline{\text{P.2}}) : \max_{\mathbf{z}, \mathbf{q}, \mathbf{P}_{\text{sar}}, \mathbf{P}_{\text{com}}} \frac{L}{\Delta_s} C(\overline{\mathbf{u}}^r)$$

s.t.

$$\overline{\text{C6}} : z_{\min} \leq \overline{z}^r(n) \leq z_{\max}, \forall n \in \mathbb{N}_N,$$

$$\overline{\text{C7}} : \text{SNR}_n(\mathbf{P}_{\text{sar}}, \overline{\mathbf{u}}^r) \geq \text{SNR}_{\min}, \forall n \in \mathbb{N}_N,$$

$$\overline{\text{C8}} : R_n(\mathbf{P}_{\text{com}}, \overline{\mathbf{u}}^r) \geq R_{\min, n}(\overline{\mathbf{u}}^r) + R_{\text{sl}}, \forall n \in \mathbb{N}_N,$$

$$\overline{\text{C9}} : 0 \leq P_{\text{sar}}(n) \leq P_{\text{sar}}^{\max}, 0 \leq P_{\text{com}}(n) \leq P_{\text{com}}^{\max}, \forall n \in \mathbb{N}_N,$$

$$\overline{\text{C10}} : q(1) = q_{\text{start}}, q(n) \geq 0, \forall n \in \mathbb{N}_N,$$

$$\overline{\text{C11}} : q(n + 1) = q(n) - M\delta_t P_{\text{tot}}(n), \forall n \in \mathbb{N}_{N-1},$$

where $\overline{z}^r(n) = z(n) + \overline{\delta}_z^r(n)$, and the UAV position in each azimuth scan n , denoted by $\overline{\mathbf{u}}^r(n)$, is given by:

$$\overline{\mathbf{u}}^r(n) = [l_n^r(\mathbf{z}), \overline{y}(n), \overline{z}^r(n)]^T, \forall n \in \mathbb{N}_N, \quad (50)$$

where $l_n^r(\mathbf{z}) = (c_2 - c_1) \sum_{k=1}^{n-1} z(k) - c_1 z(n) + \overline{\delta}_x^r(n)$. Problem $(\overline{\text{P.2}})$ is an N -dimensional non-convex non-monotonic MINLP. Next, we show that $(\overline{\text{P.2}})$ is an upper bound to problem (P.2), then, we provide the optimal solution of $(\overline{\text{P.2}})$ using monotonic optimization.

Theorem 1. *Let $\overline{\mathbf{u}}^r$ and \mathbf{u}^r be the optimal solutions to problems $(\overline{\text{P.2}})$ and (P.2), respectively, then $\frac{L}{\Delta_s} C(\overline{\mathbf{u}}^r) \geq C(\mathbf{u}^r), \forall r \in [0, 1]$. In other words, the optimal solution to problem $(\overline{\text{P.2}})$ provides an upper bound for the optimal solution to problem (P.2).*

Proof. Please refer to Appendix C. □

2) *Reformulation as Monotonic Optimization Problem:* To provide the optimal solution to problem $(\overline{\text{P.2}})$, we write the problem in the canonical form of a monotonic optimization problem given by [41], [42]:

$$\max\{\mathcal{C}(\mathbf{x}) | \mathbf{x} \in \mathcal{G} \cap \mathcal{H}\}, \quad (51)$$

where $\mathcal{C} : \mathbb{R}_+^{N \times 1} \rightarrow \mathbb{R}$ is the cost function which is increasing w.r.t. $\mathbf{x} \in \mathbb{R}^{N \times 1}$, $\mathcal{G} \subset [\mathbf{0}, \mathbf{b}] \subset \mathbb{R}_+^{N \times 1}$ is a compact normal set with non-empty interior, and \mathcal{H} is a conormal set on the box $[\mathbf{0}, \mathbf{b}]^4$. As a first step, we rewrite constraint $\overline{\text{C8}}$ as follows:

$$\overline{\text{C8}} : \left(A 2^{\alpha \bar{z}^r(n)} - 1 \right) d_n^2(\bar{\mathbf{u}}^r) - P_{\text{com}}(n) \gamma \leq 0, \forall n \in \mathbb{N}_N. \quad (52)$$

Constraint $\overline{\text{C8}}$ is non-convex and non-monotonic w.r.t. optimization variable \mathbf{z} and \mathbf{P}_{com} . Thus, we transform $\overline{\text{C8}}$ into a set of monotonic constraints by first writing it as a difference of monotonic functions.

Proposition 4. *Constraint $\overline{\text{C8}}$ is a difference of two monotonic functions $f(z(n)) - g(z(n), P_{\text{com}}(n))$, where $f(z(n))$ is given by:*

$$f(z(n)) = \left(2^{\alpha \bar{z}^r(n)} - 1 \right) \left((c_2 - c_1)^2 \left(\sum_{k=1}^{n-1} z(k) \right)^2 + 2z(n) \left(c_1 [g_x]^+ - c_1 \bar{\delta}_x^r(n) + \bar{\delta}_z^r(n) \right) + (1 + c_1^2) z^2(n) + 2(c_2 - c_1) \sum_{k=1}^{n-1} z(k) [-g_x]^+ + (g_x - \bar{\delta}_x^r(n))^2 + (g_z - \bar{\delta}_z^r(n))^2 + (\bar{y}(n) - g_y)^2 \right), \quad (53)$$

and $g(z(n), P_{\text{com}}(n))$ is given by :

$$g(z(n), P_{\text{com}}(n)) = \gamma P_{\text{com}}(n) + \left(2^{\alpha \bar{z}^r(n)} - 1 \right) \times \left(2(c_1 [-g_x]^+ + g_z) z(n) + (c_2 - c_1) (2[g_x]^+ + c_1 z(n)) \sum_{k=1}^{n-1} z(k) \right), n \in \mathbb{N}_N. \quad (54)$$

Proof. The result can be easily obtained by verifying that functions f and g are increasing w.r.t. z and $f(z(n)) - g(z(n), P_{\text{com}}(n))$ is equal to the left-hand side of (52). \square

Constraint $\overline{\text{C8}}$ is a difference of monotonic functions f and g , thereby, as proven in [41], we can equivalently represent it with the following constraints:

$$\overline{\text{C8a}} : f(z(n)) + t(n) \leq f(z_{\text{max}}), \forall n \in \mathbb{N}_N, \quad (55)$$

$$\overline{\text{C8b}} : g(z(n), P_{\text{com}}(n)) + t(n) \geq f(z_{\text{max}}), \forall n \in \mathbb{N}_N, \quad (56)$$

$$\overline{\text{C8c}} : 0 \leq t(n) \leq f(z_{\text{max}}) - f(0), \forall n \in \mathbb{N}_N, \quad (57)$$

⁴Rigorous definitions of increasing functions, boxes, normal sets, and conormal sets are provided in the monotonic optimization theory guides [41], [42].

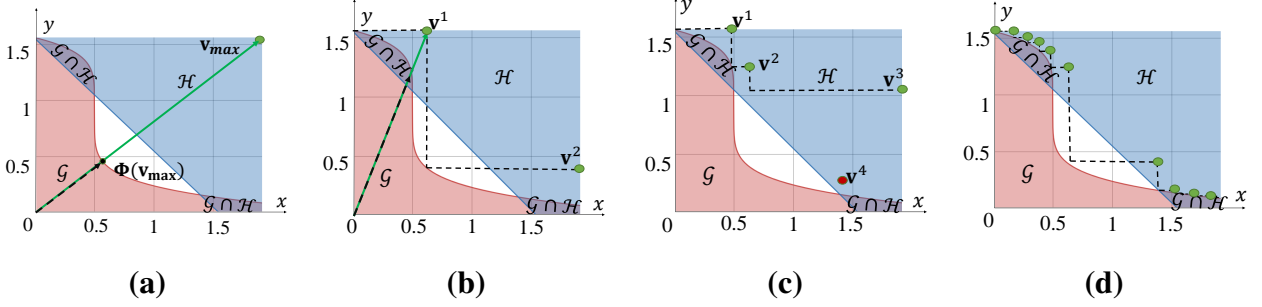


Fig. 5. Illustration of polyblock outer approximation algorithm. (a) Feasible set for a monotonic maximization problem where the normal and conormal sets are denoted by \mathcal{G} and \mathcal{H} , respectively. (b) Projection of \mathbf{v}_{\max} on normal set \mathcal{G} . (c) Projection of the best vertex $\mathbf{v}^1 = \arg \max_{\mathbf{v} \in \mathcal{T}^{(1)}} C(\mathbf{v})$ on normal set \mathcal{G} and removal of improper vertex \mathbf{v}^4 (dominated by \mathbf{v}^3). (d) Representation of a tighter polyblock obtained after several iterations.

where $\mathbf{t} = [t(1), \dots, t(N)]^T \in \mathbb{R}^{N \times 1}$ is a vector of auxiliary optimization variables. Problem $(\overline{\text{P.2}})$ can now be written in the canonical form of a monotonic optimization problem as follows:

$$\begin{aligned}
 (\overline{\text{P.3}}) : \quad & \max_{\mathbf{z}, \mathbf{t}, \mathbf{q}, \mathbf{P}_{\text{sar}}, \mathbf{P}_{\text{com}}} \frac{L}{\Delta_s} C(\overline{\mathbf{u}}^r) \\
 \text{s.t.} \quad & \overline{\text{C6}}, \overline{\text{C7}}, \overline{\text{C8a}}, \overline{\text{C8b}}, \overline{\text{C8c}}, \overline{\text{C9}}, \overline{\text{C10}}, \overline{\text{C11}},
 \end{aligned}$$

where the feasible set is the intersection of normal set \mathcal{G} that is spanned by constraints $(\overline{\text{C6}}, \overline{\text{C7}}, \overline{\text{C8a}}, \overline{\text{C8c}}, \overline{\text{C9}}, \overline{\text{C10}}, \overline{\text{C11}})$ and conormal set \mathcal{H} that is spanned by constraints $(\overline{\text{C6}}, \overline{\text{C8b}})$. The optimal solution of problem $(\overline{\text{P.3}})$ lies at the upper boundary of the normal set \mathcal{G} , denoted by $\partial^+ \mathcal{G}$ [42]. This region is not known a priori but the sequential polyblock approximation algorithm can be used to approach this set from above.

3) *Polyblock Approximation Algorithm:* In **Algorithm 2**, we provide all steps of the proposed polyblock outer approximation algorithm that generates an ϵ -approximate optimal solution to problem $(\overline{\text{P.3}})$. In addition, Figure 5 depicts the operation of the polyblock algorithm where, for simplicity of illustration, we consider a case with only two dimensions x and y . The optimization variables of problem $(\overline{\text{P.3}})$ are divided into outer optimization variables, that are collected in vertex vector $\mathbf{v} = [\overline{\mathbf{z}}^r{}^T, \mathbf{t}^T, (\mathbf{P}_{\text{com}})^T]^T \in \mathbb{R}^{3N \times 1}$, and inner optimization variables, \mathbf{q} and \mathbf{P}_{sar} . Hereinafter, as the objective function depends only on \mathbf{z} , for ease of notation, $C(\mathbf{v})$ refers to $\frac{L}{\Delta_s} C([v(1), \dots, v(N)]^T)$.

As shown in Figure 5a, first, we initialize a polyblock $\mathcal{P}^{(1)}$ with corresponding vertex set $\mathcal{T}^{(1)}$, which initially contains vertex $\mathbf{v}_{\max} = [\mathbf{z}_{\max}, \mathbf{t}_{\max}, \mathbf{P}_{\text{com}}^{\max}]^T \in \mathbb{R}^{3N \times 1}$, where $\mathbf{z}_{\max} = [z_{\max} - \overline{\delta}_z^r(1), \dots, z_{\max} - \overline{\delta}_z^r(N)] \in \mathbb{R}^{1 \times N}$, $\mathbf{t}_{\max} = [f(z_{\max}) - f(0), \dots, f(z_{\max}) - f(0)] \in \mathbb{R}^{1 \times N}$, and $\mathbf{P}_{\text{com}}^{\max} =$

Algorithm 2 Polyblock Outer Approximation Algorithm

- 1: Initialization: Set polyblock \mathcal{P}_1 with vertex $\mathbf{v}_{\max} = [\mathbf{z}_{\max}, \mathbf{t}_{\max}, \mathbf{P}_{\text{com}}^{\max}]^T$, vertex set $\mathcal{T}^{(1)} = \{\mathbf{v}_{\max}\}$, small positive number $\epsilon \geq 0$, objective function value $\text{CBV}_0 = -\infty$, and iteration number $k = 0$.
 - 2: **repeat**
 - 3: $k = k + 1$. ▷ Increment iteration index
 - 4: Select $\mathbf{v}_k = \arg \max_{\mathbf{v} \in \mathcal{T}^{(k)}} (C(\mathbf{v}))$ ▷ Select the best vertex in set $\mathcal{T}^{(k)}$
 - 5: Compute the projection $\Phi(\mathbf{v}_k)$ on $\partial\mathcal{G}^+$ using **Algorithm 3**
 - 6: **if** $\Phi(\mathbf{v}_k) = \mathbf{v}_k$, i.e., $\mathbf{v}_k \in \mathcal{G}$ **then**
 - 7: $\mathbf{s}_k = \mathbf{v}_k$ and $\text{CBV}_k = C(\Phi(\mathbf{v}_k))$
 - 8: **else**
 - 9: **if** $\Phi(\mathbf{v}_k) \in \mathcal{G} \cap \mathcal{H}$ and $C(\Phi(\mathbf{v}_k)) \geq \text{CBV}_{k-1}$ **then** ▷ Better solution is found
 - 10: Let the current best solution $\mathbf{s}_k = \Phi(\mathbf{v}_k)$ and $\text{CBV}_k = C(\Phi(\mathbf{v}_k))$ ▷ Update best solution
 - 11: **else**
 - 12: $\mathbf{s}_k = \mathbf{s}_{k-1}$ and $\text{CBV}_k = \text{CBV}_{k-1}$
 - 13: **endif**
 - 14: Set $\mathcal{T}^{(k+1)} = \{\mathcal{T}^{(k)} \setminus \mathcal{T}^*\} \cup \{\mathbf{v}^i = \mathbf{v} + ((\Phi(\mathbf{v}_k))_i - v_i)\mathbf{e}_i \mid \mathbf{v} \in \mathcal{T}^*, i \in \{1, \dots, 3N\}\}$,
 where $\mathcal{T}^* = \{\mathbf{v} \in \mathcal{T}^{(k)} \mid \mathbf{v} > \Phi(\mathbf{v}_k)\}$
 - 15: Remove from $\mathcal{T}^{(k)}$ improper vertices and vertices $\{\mathbf{v} \in \mathcal{T}^{(k+1)} \mid \mathbf{v} \notin \mathcal{H}\}$ ▷ Discard unnecessary vertices from set $\mathcal{T}^{(k+1)}$
 - 16: **endif**
 - 17: **until** $|C(\mathbf{v}_k) - \text{CBV}_k| \leq \epsilon$ ▷ Verify convergence
 - 18: **return** solution \mathbf{s}_k
-

$[P_{\text{com}}^{\max}, \dots, P_{\text{com}}^{\max}] \in \mathbb{R}^{1 \times N}$. The projection of the vertex \mathbf{v}_{\max} onto the normal set \mathcal{G} , denoted by $\Phi(\mathbf{v}_{\max}) \in \mathbb{R}^{3N \times 1}$, is calculated and used to construct a tighter polyblock $\mathcal{P}^{(2)}$, see Figure 5b. The new vertex set is calculated as $\mathcal{T}^{(2)} = \{\mathcal{T}^{(1)} \setminus \mathbf{v}_{\max}\} \cup \{\mathbf{v}^i = \mathbf{v}_{\max} + ((\Phi(\mathbf{v}_{\max}))_i - (\mathbf{v}_{\max})_i)\mathbf{e}_i, i \in \{1, \dots, 3N\}\}$, where $(\Phi(\mathbf{v}_{\max}))_i$ and $(\mathbf{v}_{\max})_i$ are the i^{th} -elements of vectors $\Phi(\mathbf{v}_{\max})$ and \mathbf{v}_{\max} , respectively. Here, \mathbf{e}_i is the unit vector whose i^{th} entry is equal to 1 and all other entries are equal to 0. Then, in iteration k , the vertex that maximizes the objective function of problem $(\overline{\text{P.3}})$

is selected to create the next polyblock, i.e., $\mathbf{v}_k = \arg \max_{\mathbf{v} \in \mathcal{T}^{(k)}} \{C(\mathbf{v})\}$. Once a feasible projection (i.e., $\Phi(\mathbf{v}_k) \in \mathcal{G} \cap \mathcal{H}$) that improves the objective function of problem $(\overline{\text{P.3}})$ is located, the corresponding vector $\mathbf{s}_k = \Phi(\mathbf{v}_k)$ and its objective function $\text{CBV}_k = C(\Phi(\mathbf{v}_k))$ are recorded. To speed up convergence and save memory, improper vertices⁵ and vertices that are not in set \mathcal{H} are removed in each iteration, e.g., vertex \mathbf{v}^4 in Figure 5c. The same procedure is repeated multiple times, such that a sequence of polyblocks converges from above to the feasible set, i.e., $\mathcal{P}^{(1)} \supset \mathcal{P}^{(2)} \supset \dots \supset \mathcal{P}^{(k)} \supset \mathcal{G} \cap \mathcal{H}$, see Figure 5d. The termination criterion of the proposed algorithm is $|C(\mathbf{v}_k) - \text{CBV}_k| \leq \epsilon$, where ϵ is the error tolerance.

Algorithm 3 Bisection Search to Compute the Upper Boundary Point

1: Initialization: Set vertex \mathbf{v} , $\lambda_{\min} = 0$, $\lambda_{\max} = 1$, and error tolerance $0 < \epsilon \ll 1$.

2: **repeat**

3: $\lambda = \frac{(\lambda_{\max} + \lambda_{\min})}{2}$ ▷ Bisection middle point

4: **if** $\lambda \mathbf{v}$ is feasible for problem $(\overline{\text{P.3}})$ **then**

5: Set $\lambda_{\min} = \lambda$ ▷ Search in $[\lambda, \lambda_{\max}]$

6: **else**

7: Set $\lambda_{\max} = \lambda$ ▷ Search in $[\lambda_{\min}, \lambda]$

8: **end if**

9: **until** $\lambda_{\max} - \lambda_{\min} \leq \epsilon$ ▷ Verify convergence

10: **return** $\Phi(\mathbf{v}) = \lambda \mathbf{v}$

In Line 4 of **Algorithm 2**, we compute the projection of vertex $\mathbf{v}_k = \arg \max_{\mathbf{v} \in \mathcal{T}^{(k)}} C(\mathbf{v})$ on $\partial \mathcal{G}^+$, denoted by $\Phi(\mathbf{v}_k) \in \mathbb{R}^{3N \times 1}$. This projection is not trivial and is equivalent to solving a one-dimensional optimization problem: $\max_{0 \leq \lambda \leq 1} \{\lambda \mathbf{v}_k \in \mathcal{G}\}$. To compute $\Phi(\mathbf{v}_k)$, we perform a bisection search using **Algorithm 3**. In each iteration of **Algorithm 3**, checking if a vector belongs to the normal set \mathcal{G} is equivalent to solving problem $(\overline{\text{P.3}})$ when fixing the outer optimization variables, i.e., vectors \mathbf{z} , \mathbf{t} , and \mathbf{P}_{com} . This results in the following feasibility problem:

$$\begin{aligned}
 (\overline{\text{P.4}}) : & \max_{\mathbf{q}, \mathbf{P}_{\text{sar}}} 1 \\
 \text{s.t.} & \quad \overline{\text{C7}}, \overline{\text{C9}}, \overline{\text{C10}}, \overline{\text{C11}}.
 \end{aligned}$$

⁵Given a vertex set \mathcal{T} , improper vertices are vertices that are dominated by other vertices in \mathcal{T} . See Figure 5c and [41] for further details.

TABLE II
SYSTEM PARAMETERS [16], [34], [43].

Parameter	Value	Parameter	Value
L	60 m	$\mathbf{g} = [g_x, g_y, g_z]^T$	$[0, 0, 5]^T$ m
M	100	v	5 m/s
z_{\max} and z_{\min}	100 m and 2 m	q_{start}	19.44 Wh
P_{sar}^{\max}	46 dBm	P_{prop}	450 W
P_{com}^{\max}	40 dBm	P_0	79.86 W
θ_d and $\theta_{3\text{db}}$	45° and 30°	P_I	420.6 W
τ_p and PRF	1 μs and 100 Hz	W_u	56.5 N
B_r	100 MHz	U_{tip}	120 m/s
B_c	100 MHz	ρ	1.225 kg/m ³
f	2 GHz	A	0.503 m ²
SNR_{\min}	20 dB	d_0	0.6
R_{sl}	1 kbit	s	0.05
γ	20 dB	β	$10^4 \text{ W}^{-1} \text{ m}^3$

Problem $(\overline{\text{P.4}})$ is a convex optimization problem and a feasible solution can be obtained by, e.g., CVX [37]. Once the projection point is computed, the new polyblock is generated as described previously and these steps are repeated until the optimal solution is located.

The computational complexity of the upper bound on the optimal solution, provided by **Algorithm 2** and **Algorithm 3**, is exponential in the number of vertex elements, i.e., the time complexity order is $O(2^{3N})$ [42]. If problem $(\overline{\text{P.2}})$ is feasible, then **Algorithm 2** converges to its global optimal solution as the polyblock approximation algorithm has been proven to converge to an ϵ -optimal solution [42]. Despite the high complexity of the derived upper bound, it can be used to assess the performance of the proposed low-complexity sub-optimal scheme.

V. SIMULATION RESULTS AND DISCUSSION

In this section, we present simulation results for the proposed robust UAV 3D trajectory and resource allocation algorithm, where we adopted the parameter values provided in Table II, unless specified otherwise. The minimum UAV altitude z_{\min} was set to 2 m to avoid crashes due to collisions with obstacles at very low altitudes. For all robust schemes, we adopt the Gaussian model for the UAV trajectory deviations where in-range position errors follow $\mathcal{N}(o_x = 1 \text{ m}, \sigma = 0.3 \text{ m})$ and altitude errors follow $\mathcal{N}(o_z = -1 \text{ m}, \sigma = 0.3 \text{ m})$.

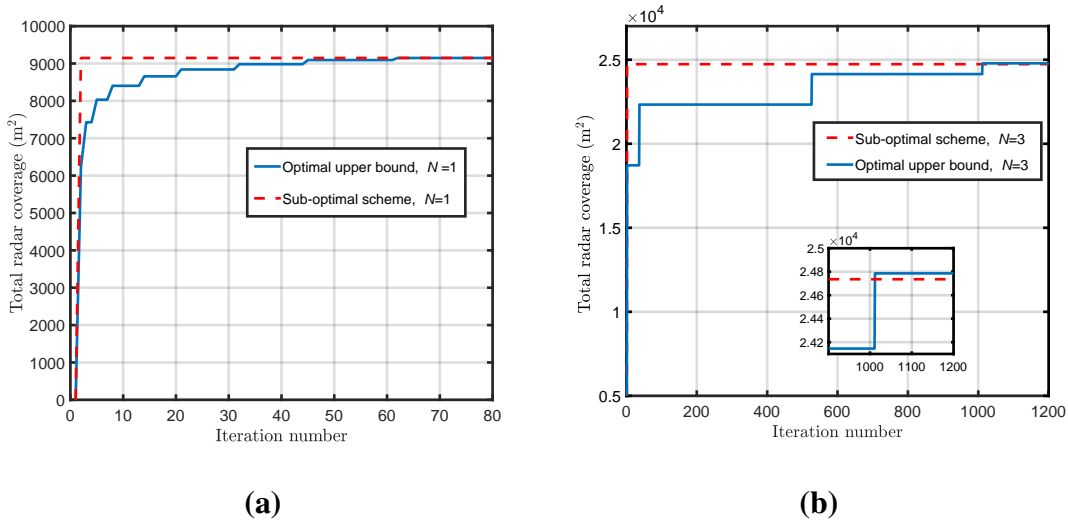


Fig. 6. Convergence of algorithm 1 (sub-optimal) and algorithm 2 (upper bound) for $N = 1$ (a) and $N = 3$ (b).

A. Benchmark Schemes

To evaluate the performance of the proposed robust scheme, we compare it with the following benchmark schemes:

- **Benchmark scheme 1:** This is a non-robust scheme, where we solve problem (P.1) assuming no UAV trajectory deviations, i.e., $\sigma = 0$, $o_x = 0$, and $o_z = 0$. This benchmark scheme was presented in [1] where $\mathbf{u}^r = \mathbf{u}$.
- **Benchmark scheme 2:** This is a robust scheme, where we solve problem (P.1) assuming the communication power P_{com} is fixed across all time slots and optimized along with the other optimization variables. The coverage reliability level is $r = 0.95$.
- **Benchmark scheme 3:** This is also a robust scheme, with $r = 0.95$, where we solve problem (P.1) assuming the SAR power P_{sar} is fixed across all time slots but optimized along with the other optimization variables.

We note that all benchmark schemes have polynomial time complexity, similar to the proposed sub-optimal scheme.

B. Convergence and Accuracy of the Proposed Scheme

In Figure 6, we analyze the convergence rate of the proposed sub-optimal and optimal (upper bound) schemes for different numbers of azimuth sweeps N . We also assess the gap between the optimal and sub-optimal solutions. The results are plotted as a function of the iteration number of

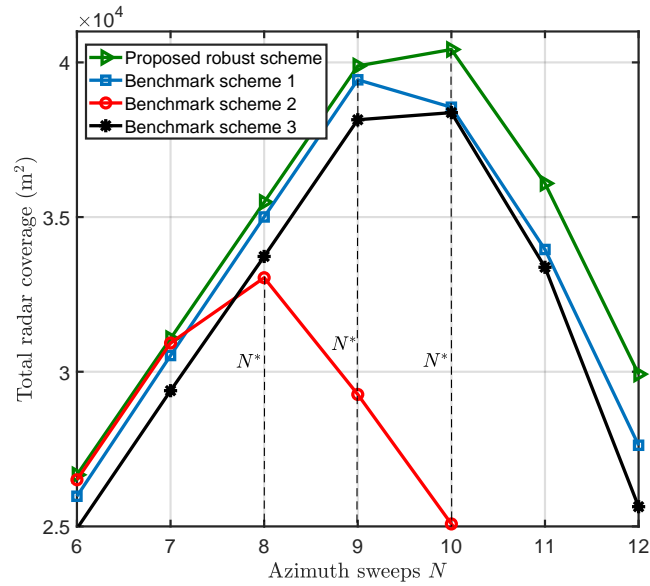


Fig. 7. Comparison of the radar coverage of the considered schemes.

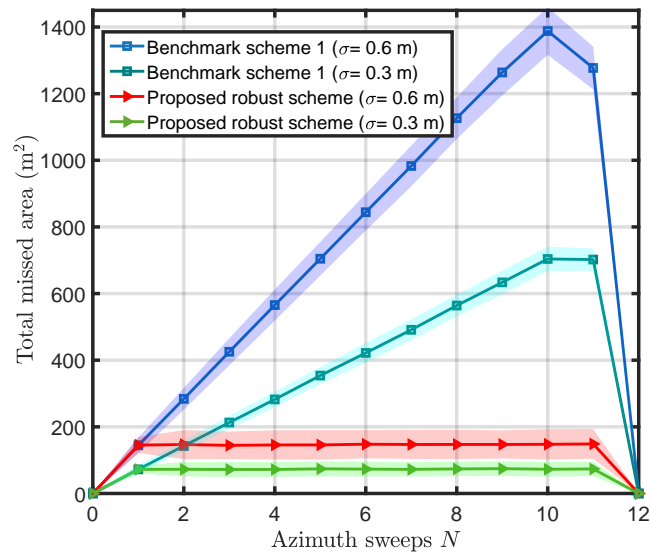


Fig. 8. Total missed area of the proposed robust scheme compared to the non-robust scheme for different trajectory deviation levels. Shaded area represents one standard deviation while solid line represents the mean value averaged over 10^4 realizations.

Algorithm 1 and **Algorithm 2**, respectively. Figure 6 shows that the proposed scheme converges fast to the upper bound on the optimal solution given by $C(z^*) \approx 9.154 \times 10^3 \text{ m}^2$ for $N = 1$, and $C(z^*) \approx 2.496 \times 10^4 \text{ m}^2$ for $N = 3$. After convergence, the gap between the upper bound on the optimal solution and the sub-optimal solution is negligible which confirms that the proposed sub-optimal scheme achieves close-to-optimal performance with low complexity.

In Figure 7, we depict the sensing coverage as a function of the number of azimuth sweeps N . The figure illustrates how the optimal N^* , leading to the best possible coverage, can be obtained based on a finite exhaustive search. Furthermore, we compare the proposed scheme with the benchmark schemes. In fact, the figure illustrates the superior performance of the proposed robust scheme over robust benchmark schemes 2 and 3. The gain is attributed to the optimization of the communication power and radar transmit power, respectively. In comparison to non-robust benchmark scheme 1, our proposed robust scheme achieves comparable or improved coverage depending on the system parameters. Yet, the advantage of the proposed robust scheme over the non-robust scheme is illustrated in Figure 8, which shows the total area missed by the UAV (i.e., the total area of all holes in the total coverage) averaged over 10^4 realizations and for different levels of random trajectory deviations. For the non-robust design, the missed area increases with the number of total azimuth sweeps, as more area is missed by the UAV-SAR due to random trajectory deviations. However, the proposed robust design keeps the missed area small and constant for different numbers of azimuth sweeps to ensure that the required $r = 95\%$ coverage reliability is achieved. This confirms that, in terms of total missed area, the robust scheme outperforms the non-robust scheme, as the latter may cause significant coverage holes and thus, is not suitable in practice.

C. Robustness of the Proposed Design Against UAV Trajectory Deviations

In Figure 9, we investigate the effect of UAV trajectory deviations on SAR mapping for low-altitude radar applications (i.e., $z_{\max} = 10 \text{ m}$). In Figure 9a, the dashed red line denotes the non-robust UAV trajectory provided by benchmark scheme 1, whereas the solid blue line shows the actual UAV flight path. In Figure 9b, we show the resulting UAV-SAR ground coverage with green- and yellow-colored rectangles denoting successive azimuth scans. Following an ideal path planning, the expected covered area is measured by the dashed red rectangle. However, the actual covered area is different from the expected result. Figure 9b shows how small flight deviations can affect the UAV coverage, where the total uncovered area for benchmark scheme 1 was 225

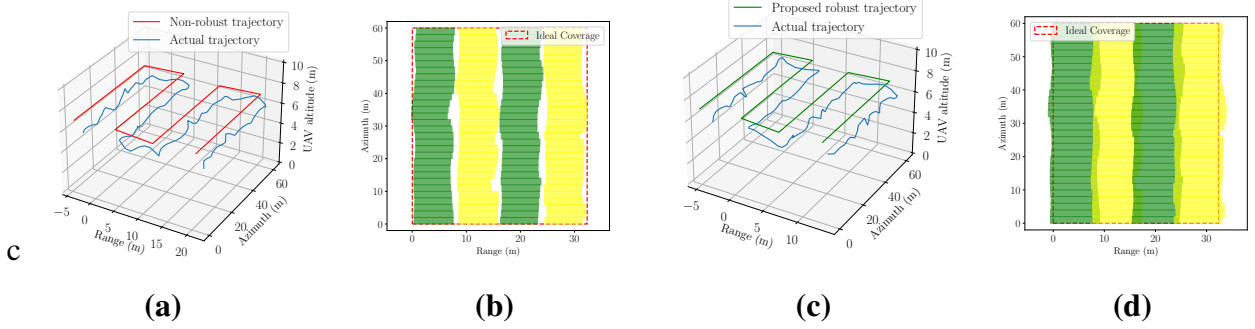


Fig. 9. Robust versus non-robust UAV trajectory design. (a) Non-robust 3D UAV trajectory for optimized coverage. (b) Actual 2D ground SAR coverage following the trajectory shown in (a). (c) Robust UAV trajectory for optimized coverage. (d) Actual 2D ground SAR coverage following the trajectory shown in (c).

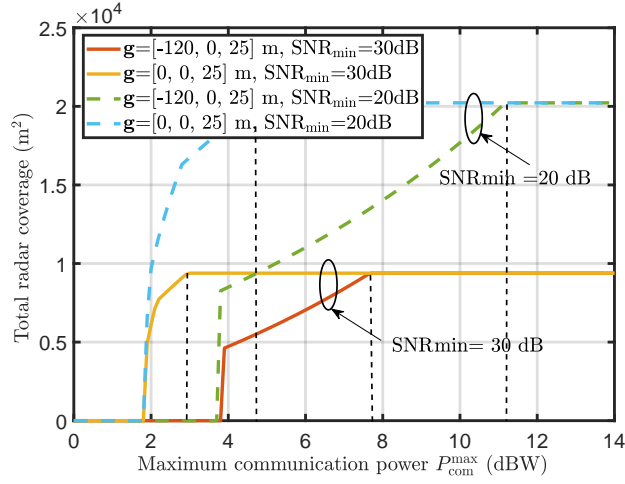


Fig. 10. Total radar coverage versus maximum communication power.

m^2 out of $C(\mathbf{z}) = 1.859 \times 10^3 \text{ m}^2$ (12%). In Figure 9c, we present the proposed robust UAV trajectory with a solid green line. Figure 9d highlights the tradeoff between coverage performance and robustness for low-altitude sensing applications. Although the total coverage is comparable, the proposed robust scheme is highly effective in avoiding uncovered areas caused by random UAV trajectory deviations, as any location in the AoI is guaranteed to be covered with a 95% probability.

D. Real-time Communication

In Figure 10, we plot the total radar ground coverage as a function of the UAV's maximum communication power for different placements of the GS and different required radar SNR values.

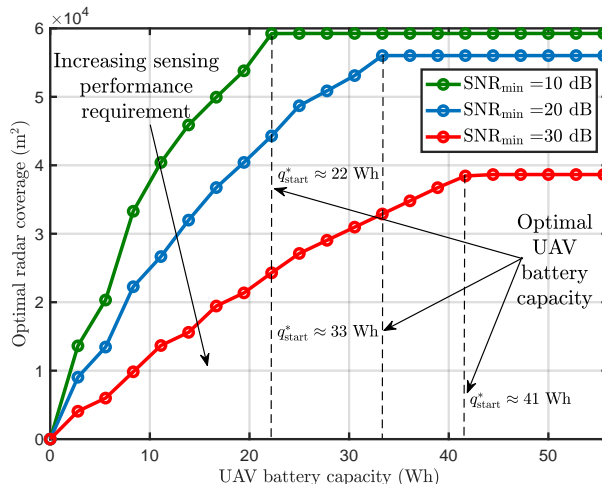


Fig. 11. Total radar coverage versus UAV battery capacity for different sensing requirements.

This figure highlights the impact of communication on the sensing performance. In particular, the communication transmit power affects the UAV trajectory (see (16)), and therefore also the sensing performance, as the trajectory of the drone is linked to the ground coverage and the sensing SNR through (11) and (14), respectively. Figure 10 shows that, when the GS is far from the AoI, i.e., for $\mathbf{g} = [-120, 0, 25]$ m, the total coverage is reduced as the minimum required data rate cannot be achieved at distances far from the GS due to the increased path loss. This can be compensated by increasing the maximum UAV transmit power. In fact, for sufficiently high maximum UAV transmit powers, the radar SNR constraint becomes the performance bottleneck causing the total coverage to saturate. For instance, as shown in Figure 10, a maximum UAV communication power of $P_{\text{com}}^{\text{max}} = 7.78$ dBW results in the best possible radar coverage when $\text{SNR}_{\text{min}} = 30$ dB and $\mathbf{g} = [-120, 0, 25]$ m. In a nutshell, a reliable data backhaul link is crucial for enabling real-time on-ground processing of SAR data.

E. Impact of UAV Battery Capacity on Sensing Performance

In Figure 11, we depict the SAR coverage as a function of the UAV battery capacity for different required sensing SNRs, SNR_{min} . The figure shows that the optimum SAR coverage increases with the battery capacity and saturates for a certain value denoted by q_{start}^* , which is the minimum UAV battery capacity needed to achieve maximum coverage for a given required sensing SNR. The coverage can not be further improved by increasing q_{start} beyond q_{start}^* due to

communication constraint C8, which eventually becomes the performance bottleneck for large UAV-GS distances. In addition, Figure 11 reveals that for more stringent sensing requirements, not only does the total coverage decrease, but the energy needed to achieve maximum coverage also increases. This is because the flying altitude has to be reduced to satisfy more stringent SNR requirements leading to less coverage. However, when the UAV is forced to fly at lower altitudes, a larger number of sweeps have to be performed to maximize the coverage, which results in a higher energy consumption. For example, for $\text{SNR}_{\min} = 10$ dB, $C(z^*) = 5.9 \times 10^4$ m² is obtained with a 22 Wh battery capacity, whereas for $\text{SNR}_{\min} = 30$ dB, only $C(z^*) = 3.8 \times 10^4$ m² is achieved requiring almost twice the battery capacity, i.e., 41 Wh. This further shows that the limited energy available to small UAVs, which is accounted for by constraints C9 – C11, has a significant impact on sensing performance.

VI. CONCLUSION

In this paper, we investigated robust joint 3D trajectory and resource allocation design for UAV-SAR systems, where real-time transmission of radar data to the ground was taken into account. Random UAV trajectory deviations were modeled and their effect on the ground radar coverage was derived based on their statistics. Moreover, the robust 3D trajectory and resource allocation design was formulated as a mixed-integer non-linear optimization problem for maximization of the UAV radar coverage. A low-complexity sub-optimal solution based on SCA was provided. To assess the performance of the proposed algorithm, we derived an upper bound for the optimal solution based on monotonic optimization theory. Simulation results confirmed that the proposed robust sub-optimal solution achieves close-to-optimal performance. The superior performance of the proposed scheme compared to three benchmark schemes was established and the robustness of the proposed solution w.r.t. UAV trajectory deviations was confirmed. Finally, we highlighted the impact of GS placement and the power available for communication on UAV radar performance. In this paper, we assumed a deterministic LOS link between the UAV and the GS. An interesting topic for future work is the extension to other types of air-to-ground channels, including Ricean fading channels, based on online optimization techniques, see, e.g., [39]. Furthermore, while we used classical optimization methods and focused on single-UAV SAR sensing, the extension to multi-UAV SAR sensing [44] and the exploration of learning-based methods for the trajectory design and resource allocation are promising research directions.

APPENDIX A

PROOF OF PROPOSITION 1

Assuming Gaussian UAV position deviations, i.e., $\Delta_x(n) \sim \mathcal{N}(o_x, \sigma)$ and $\Delta_z(n) \sim \mathcal{N}(o_z, \sigma)$, and using (20) and (21), we can show that $\Delta_{\mathbf{p}_N}(n) \sim \mathcal{N}(o_x + c_1 o_z, \sigma\sqrt{1+c_1^2})$ and $\Delta_{\mathbf{p}_F}(n) \sim \mathcal{N}(o_x + c_2 o_z, \sigma\sqrt{1+c_2^2}), \forall n \in \mathbb{N}_{NM}$. In time slot n , let set $\mathcal{I}_N = \{s \in \mathbb{R} \mid \mathbb{P}(\Delta_{\mathbf{p}_N}(n) + s \leq 0) \geq r\}$, where r is the coverage reliability. Based on the definition of the near-range and far-range compensation provided in (22) and (23), respectively, we can write:

$$F_{\Delta_{\mathbf{p}_N}(n)}(-s) \geq r, \quad (58)$$

$$1 - F_{-\Delta_{\mathbf{p}_N}(n)}(s) \geq r, \quad (59)$$

$$\frac{1}{2} \left(1 - \operatorname{erf} \left(\frac{s + o_x + c_1 o_z}{\sigma\sqrt{2(1+c_1^2)}} \right) \right) \geq r, \quad (60)$$

$$\operatorname{erf} \left(\frac{s + o_x + c_1 o_z}{\sigma\sqrt{2(1+c_1^2)}} \right) \leq 1 - 2r. \quad (61)$$

Since the inverse of the error function, denoted by $\operatorname{erf}^{-1}(\cdot)$, is an increasing function, we have:

$$s \leq h_{\mathbf{p}_N}(r), \quad (62)$$

where $h_{\mathbf{p}_N}(r) = \operatorname{erf}^{-1}(1 - 2r)\sigma\sqrt{2(1+c_1^2)} - o_x - c_1 o_z$. Then, the required near-range compensation $\delta_{\mathbf{p}_N}^r(n) = \arg \min(|s|)$ is given by:

$$\delta_{\mathbf{p}_N}^r(n) = \begin{cases} 0 & \text{if } h_{\mathbf{p}_N}(r) \geq 0, \\ h_{\mathbf{p}_N}(r) & \text{if } h_{\mathbf{p}_N}(r) \leq 0, \end{cases} \quad (63)$$

which can be equivalently written as follows:

$$\delta_{\mathbf{p}_N}^r(n) = \min(0, h_{\mathbf{p}_N}(r)) = -[-h_{\mathbf{p}_N}(r)]^+. \quad (64)$$

This gives the final result in (24). The far-range compensation, denoted by $\delta_{\mathbf{p}_N}^r(n)$, is derived using the same methodology.

APPENDIX B

PROOF OF PROPOSITION 3

To show that the set of feasible azimuth scans is finite, we prove that N is upper bounded. From constraints C9 and C11, we obtain the following inequality:

$$\delta_t P_{\text{prop}} \leq q(n) - q(n+1), \forall n \in \mathbb{N}_{NM-1}. \quad (65)$$

The summation of both sides of (65) yields:

$$\sum_{n=1}^{NM-1} \delta_t P_{\text{prop}} \leq q(1) - q(NM) \leq q_{\text{start}}. \quad (66)$$

The result in (66) can be rigorously proven using induction applied to the telescoping series $q(n) - q(n+1)$ and constraint C10. Since the drone flies at a constant velocity v and P_{prop} is constant, we obtain an upper bound on N as follows:

$$N \leq \frac{1}{M} \left(\frac{q_{\text{start}}}{\delta_t P_{\text{prop}}} + 1 \right). \quad (67)$$

Problem (P.1) is infeasible for N exceeding the upper bound provided in (67) as this would violate constraint C11.

APPENDIX C

PROOF OF THEOREM 1

In this proof, we show that problem $(\overline{\text{P.2}})$ is an upper bound to problem (P.2). To this end, we introduce an intermediate problem, denoted by (P.2'), that provides an upper bound for problem (P.2), then we prove that problems (P.2') and $(\overline{\text{P.2}})$ are equivalent. This means that $(\overline{\text{P.2}})$ is an upper bound to the original problem (P.2). We start by rewriting constraint C8 as follows:

$$\text{C8} : g_1(n) \leq -g_2(n)(y(n) - g_y)^2, \forall n \in \mathbb{N}_{NM}, \quad (68)$$

where functions g_1 and g_2 are respectively given by:

$$g_1(n) = g_2(n) \left((x^r(n) - g_x)^2 + (z^r(n) - g_z)^2 \right) - P_{\text{com}}(n)\gamma, \quad (69)$$

$$g_2(n) = A2^{\alpha z^r(n)} - 1, \forall n \in \mathbb{N}_{NM}. \quad (70)$$

As proposed in (47), we lower bound the term $(y(n) - g_y)^2$ in (68) by taking its minimum value for each azimuth scan. Since $g_2(n) \geq 0, \forall n \in \mathbb{N}_{NM}$, by bounding $(y(n) - g_y)^2$, the right-hand side value in (68) increases. This is equivalent to relaxing constraint C8, which we denote now by $\overline{\text{C8}}$:

$$\overline{\text{C8}} : g_1(n) \leq -g_2(n) \min_{1+(n-1)M \leq k \leq nM} (y(k) - g_y)^2, \forall n \in \mathbb{N}_N. \quad (71)$$

Let us denote problem (P.2) after relaxing constraint C8 by (P.2'). It is easy to show that (P.2') provides an upper bound to problem (P.2). In fact, any feasible solution to (P.2) is also feasible for (P.2') as the solution necessarily satisfies $\overline{\text{C8}}$. Now, let us denote the optimal

altitudes to problem (P.2) and (P.2') by $\mathbf{z} \in \mathbb{R}^{NM \times 1}$ and $\mathbf{z}_2 \in \mathbb{R}^{NM \times 1}$, respectively, and their robust trajectories by \mathbf{u}^r and \mathbf{u}_2^r , respectively. Since the objective function is increasing w.r.t. altitude vector \mathbf{z} , then, relaxing C8 results in the following inequality:

$$C(\mathbf{u}^r) \leq C(\mathbf{u}_2^r), \forall r \in [0, 1]. \quad (72)$$

In the remainder of this proof, we show that problems (P.2') and $(\overline{\text{P.2}})$ are equivalent.

We apply a series of transformations to transform NM -dimensional problem (P.2') to the N -dimensional problem $(\overline{\text{P.2}})$. In fact, based on $\overline{\text{C8}}$, where the UAV-GS distance varies from scan to scan, we remark that all optimization variables of problem (P.2') are also constant for a given azimuth scan and only change from scan to scan. This allows us to reduce the dimension of the problem as optimization along the azimuth direction has no impact. Therefore, constraints C3 – C5 are dropped as they define equalities for time slots of the same azimuth scans. The rest of the constraints are now specified for each scan and denoted by $\overline{\text{C6}} – \overline{\text{C11}}$. We use N -dimensional optimization variables, where based on $\overline{\text{C8}}$ and constraints C1 and C2, optimization vector $\overline{\mathbf{x}} \in \mathbb{R}^{N \times 1}$ can be dropped from the optimization problem (P.2') as it is deterministic and can be calculated from vector $\overline{\mathbf{z}} \in \mathbb{R}^{N \times 1}$ as follows:

$$\overline{x}(n) = (c_2 - c_1) \sum_{k=1}^{n-1} \overline{z}(k) - c_1 \overline{z}(n), n \in \mathbb{N}_N. \quad (73)$$

Finally, we obtain the following relation between the objective functions of problems (P.2') and $(\overline{\text{P.2}})$:

$$C(\mathbf{u}_2^r) = \sum_{n=1}^{NM} \Delta_s (z_2(n) + \delta_z^r(n)) (c_2 - c_1) \quad (74)$$

$$\stackrel{\text{C4}}{=} L \sum_{k=1}^N \left(z_2(1 + (1 - k)M) + \delta_z^r(1 + (1 - k)M) \right) (c_2 - c_1) \quad (75)$$

$$= \frac{L}{\Delta_s} \sum_{n=1}^N \Delta_s \overline{z}^r(n) (c_2 - c_1) = \frac{L}{\Delta_s} C(\overline{\mathbf{u}}^r). \quad (76)$$

Based on (72) and (76), problem (P.2') is equivalently transformed to problem $(\overline{\text{P.2}})$, with $C(\mathbf{u}^r) \leq C(\mathbf{u}_2^r) = \frac{L}{\Delta_s} C(\overline{\mathbf{u}}^r)$, which concludes the proof.

REFERENCES

- [1] M.-A. Lahmeri, W. Ghanem, C. Knill, and R. Schober, "Trajectory and resource optimization for UAV synthetic aperture radar," in *Proc. IEEE Global Commun. Conf.*, Dec. 2022, pp. 897–903.

- [2] A. Moreira, P. Prats-Iraola, M. Younis, G. Krieger, I. Hajnsek, and K. P. Papathanassiou, "A tutorial on synthetic aperture radar," *IEEE Geosci. Remote Sens. Mag.*, vol. 1, no. 1, pp. 6–43, Mar. 2013.
- [3] D. C. Munson, J. D. O'Brien, and W. K. Jenkins, "A tomographic formulation of spotlight-mode synthetic aperture radar," *Proc. IEEE*, vol. 71, no. 8, pp. 917–925, Aug. 1983.
- [4] L. Ulander, H. Hellsten, and G. Stenstrom, "Synthetic-aperture radar processing using fast factorized back-projection," *IEEE Trans. Aerosp. Electron. Syst.*, vol. 39, no. 3, pp. 760–776, Jul. 2003.
- [5] P. A. Rosen, S. Hensley, I. R. Joughin, F. K. Li, S. N. Madsen, E. Rodriguez, and R. M. Goldstein, "Synthetic aperture radar interferometry," *Proc. IEEE*, vol. 88, no. 3, pp. 333–382, Mar. 2000.
- [6] X. X. Zhu and R. Bamler, "Very high resolution spaceborne SAR tomography in urban environment," *IEEE Trans. Geosci. Remote Sens.*, vol. 48, no. 12, pp. 4296–4308, Jun. 2010.
- [7] F. Natterer, *The Mathematics of Computerized Tomography*. SIAM, 2001.
- [8] M. Wielage, F. Cholewa, C. Fahnemann, P. Pirsch, and H. Blume, "High performance and low power architectures: GPU vs. FPGA for fast factorized backprojection," in *Proc. Int. Symp. Comput. Netw. (CANDAR)*, Nov. 2017, pp. 351–357.
- [9] R. Que, O. Ponce, R. Scheiber, and A. Reigber, "Real-time processing of SAR images for linear and non-linear tracks," in *Proc. Int. Radar Symp. (IRS)*, May 2016, pp. 1–4.
- [10] Y. Zeng, R. Zhang, and T. J. Lim, "Wireless communications with unmanned aerial vehicles: opportunities and challenges," *IEEE Commun. Mag.*, vol. 54, no. 5, pp. 36–42, May 2016.
- [11] M.-A. Lahmeri, M. A. Kishk, and M.-S. Alouini, "Artificial intelligence for UAV-enabled wireless networks: A survey," *IEEE Open J. Commun. Soc.*, vol. 2, pp. 1015–1040, Apr. 2021.
- [12] M. Z. Chowdhury, M. Shahjalal, S. Ahmed, and Y. M. Jang, "6G wireless communication systems: Applications, requirements, technologies, challenges, and research directions," *IEEE Open J. Commun. Soc.*, vol. 1, pp. 957–975, 2020.
- [13] D. Xu, Y. Sun, D. W. K. Ng, and R. Schober, "Robust resource allocation for UAV systems with UAV jittering and user location uncertainty," in *Proc. IEEE Global Commun. Conf.* IEEE, Dec. 2018, pp. 1–6.
- [14] W. Wang and W. Zhang, "Jittering effects analysis and beam training design for UAV millimeter wave communications," *IEEE Trans. Wireless Commun.*, vol. 21, no. 5, pp. 3131–3146, May 2022.
- [15] D. Xu, Y. Sun, D. W. K. Ng, and R. Schober, "Multiuser MISO UAV communications in uncertain environments with no-fly zones: Robust trajectory and resource allocation design," *IEEE Trans. Commun.*, vol. 68, no. 5, Jan. 2020.
- [16] M.-A. Lahmeri, M. A. Kishk, and M.-S. Alouini, "Laser-powered UAVs for wireless communication coverage: A large-scale deployment strategy," *IEEE Trans. Wireless Commun.*, vol. 22, no. 1, pp. 518–533, Jan. 2022.
- [17] L. Yang, J. Qi, J. Xiao, and X. Yong, "A literature review of UAV 3D path planning," in *Proc. of the 11th World Congress on Intelligent Control and Automation*, Jun. 2014, pp. 2376–2381.
- [18] Y. Huang *et al.*, "Cognitive UAV communication via joint maneuver and power control," *IEEE Trans. Commun.*, vol. 67, no. 11, pp. 7872–7888, 2019.
- [19] Q. Wu, Y. Zeng, and R. Zhang, "Joint trajectory and communication design for multi-UAV enabled wireless networks," *IEEE Trans. Wireless Commun.*, vol. 17, no. 3, pp. 2109–2121, 2018.
- [20] H. Bayerlein, M. Theile, M. Caccamo, and D. Gesbert, "Multi-UAV path planning for wireless data harvesting with deep reinforcement learning," *IEEE Open J. Commun. Soc.*, vol. 2, pp. 1171–1187, 2021.
- [21] A. Hajjamali Arani *et al.*, "Reinforcement learning for energy-efficient trajectory design of UAVs," *IEEE Internet Things Journ.*, vol. 9, no. 11, pp. 9060–9070, 2022.
- [22] M. Lort, A. Aguasca, C. Lopez-Martinez, and T. M. Marín, "Initial evaluation of SAR capabilities in UAV multicopter platforms," *IEEE J. Sel. Top. Appl. Earth Obs. and Remote Sens.*, vol. 11, no. 1, pp. 127–140, Jan. 2018.

- [23] M. G. Fernández, Y. Á. López, A. A. Arboleya, B. G. Valdés, Y. R. Vaqueiro, F. L.-H. Andrés, and A. P. García, “Synthetic aperture radar imaging system for landmine detection using a ground penetrating radar on board a unmanned aerial vehicle,” *IEEE Access*, vol. 6, pp. 45 100–45 112, 2018.
- [24] R. Burr, M. Schartel, A. Grathwohl, W. Mayer, T. Walter, and C. Waldschmidt, “UAV-borne FMCW InSAR for focusing buried objects,” *IEEE Geosci. Remote Sens. Lett.*, vol. 19, pp. 1–5, Jul. 2021.
- [25] Z. Sjanic and F. Gustafsson, “Simultaneous navigation and synthetic aperture radar focusing,” *IEEE Trans. Aerosp. Electron. Syst.*, vol. 51, no. 2, pp. 1253–1266, Apr. 2015.
- [26] S. Hu, X. Yuan, W. Ni, and X. Wang, “Trajectory planning of cellular-connected UAV for communication-assisted radar sensing,” *IEEE Trans. Commun.*, vol. 70, no. 9, pp. 6385–6396, Sep. 2022.
- [27] Z. Sun, G. G. Yen, J. Wu, H. Ren, H. An, and J. Yang, “Mission planning for energy-efficient passive UAV radar imaging system based on substage division collaborative search,” *IEEE Trans. Cybern.*, vol. 53, no. 1, pp. 275–288, Jan. 2023.
- [28] Z. Sun, J. Wu, J. Yang, Y. Huang, C. Li, and D. Li, “Path planning for GEO-UAV bistatic SAR using constrained adaptive multiobjective differential evolution,” *IEEE Trans. Geosci. Remote Sens.*, vol. 54, no. 11, pp. 6444–6457, Nov. 2016.
- [29] H. Cruz, M. Véstias, J. Monteiro, H. Neto, and R. P. Duarte, “A review of synthetic-aperture radar image formation algorithms and implementations: a computational perspective,” *Remote Sens.*, vol. 14, no. 5, p. 1258, Mar. 2022.
- [30] R. Bähneemann, N. Lawrance, L. Streichenberg, J. J. Chung, M. Pantic, A. Grathwohl, C. Waldschmidt, and R. Siegwart, “Under the sand: Navigation and localization of a micro aerial vehicle for landmine detection with ground-penetrating synthetic aperture radar,” *J. Field Robot.*, vol. 2, no. 1, pp. 1028–1067, Jun. 2022.
- [31] M. Younis, “Digital beam-forming for high resolution wide swath real and synthetic aperture radar,” Ph.D. dissertation, Zugl.: Karlsruhe, Univ., Diss., 2004.
- [32] S. Y. Kim, N. H. Myung, and M. J. Kang, “Antenna mask design for SAR performance optimization,” *IEEE Geosci. Remote Sens. Lett.*, vol. 6, no. 3, pp. 443–447, Jul. 2009.
- [33] A. Goldsmith, *Wireless Communications*. Cambridge University Press, 2005.
- [34] Y. Zeng, J. Xu, and R. Zhang, “Energy minimization for wireless communication with rotary-wing UAV,” *IEEE Trans. Wireless Commun.*, vol. 18, no. 4, pp. 2329–2345, 2019.
- [35] M. Łabowski, P. Kaniewski, and S. Konatowski, “Estimation of flight path deviations for SAR radar installed on UAV,” *Metrology and Measurement Systems*, vol. 23, no. 3, 2016.
- [36] L. Zhang, Z. Qiao, M.-d. Xing, L. Yang, and Z. Bao, “A robust motion compensation approach for UAV SAR imagery,” *IEEE Trans. Geosci. Remote Sens.*, vol. 50, no. 8, pp. 3202–3218, Feb. 2012.
- [37] M. Grant and S. Boyd, “CVX: Matlab software for disciplined convex programming, version 2.1,” Mar. 2014. [Online]. Available: <http://cvxr.com/cvx>
- [38] Q. T. Dinh and M. Diehl, “Local convergence of sequential convex programming for nonconvex optimization,” in *Recent Advances in Optimization and its Applications in Engineering: The 14th Belgian-French-German Conf. on Optimization*. Springer, 2010, pp. 93–102.
- [39] Y. Sun, D. Xu, D. W. K. Ng, L. Dai, and R. Schober, “Optimal 3D-trajectory design and resource allocation for solar-powered UAV communication systems,” *IEEE Trans. Commun.*, vol. 67, no. 6, pp. 4281–4298, Feb. 2019.
- [40] M. Hua *et al.*, “3D UAV trajectory and communication design for simultaneous uplink and downlink transmission,” *IEEE Trans. Commun.*, vol. 68, no. 9, pp. 5908–5923, 2020.
- [41] H. Tuy, “Monotonic optimization: Problems and solution approaches,” *SIAM J. Optim.*, vol. 11, no. 2, pp. 464–494, Nov. 2000.
- [42] Y. J. A. Zhang, L. Qian, J. Huang *et al.*, “Monotonic optimization in communication and networking systems,” *Found. Trends Netw.*, vol. 7, no. 1, pp. 1–75, Oct. 2013.

- [43] M. Schartel, R. Burr, W. Mayer, N. Docci, and C. Waldschmidt, "UAV-based ground penetrating synthetic aperture radar," in *Proc. IEEE MTT-S Int. Conf. Microw. Intell. Mobil.*, Apr. 2018, pp. 1–4.
- [44] M.-A. Lahmeri *et al.*, "UAV Formation Optimization for Communication-assisted InSAR Sensing," *accepted for presentation at IEEE Intern. Conf. Commun. (ICC) 2024*, *arXiv preprint arXiv:2311.06959*.